Assessment of Right Ventricle Morphology and Function in Tetralogy of Fallot using 3D Echocardiography

Using regional curvature and directionally decomposed ejection fraction

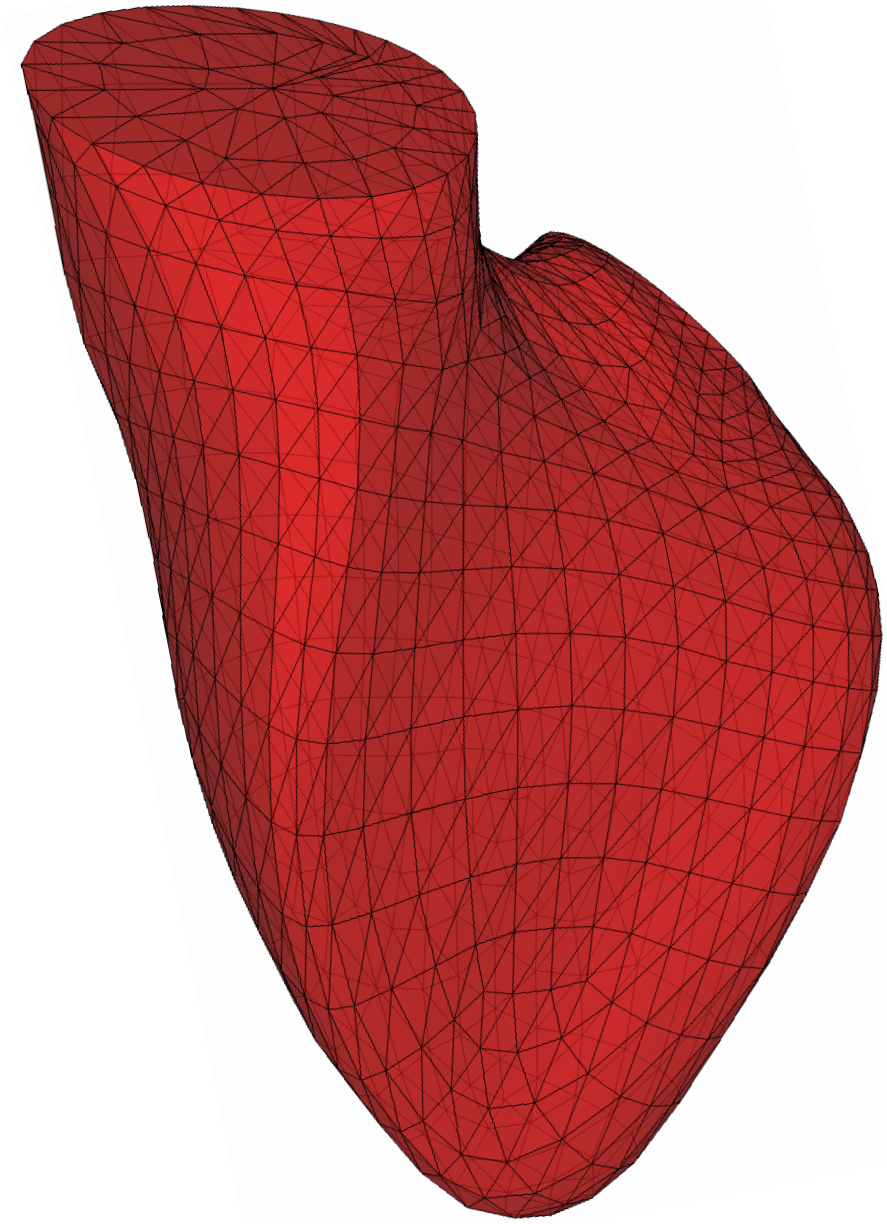

J.W. (Jop) Schneijdenberg

Master Thesis Technical Medicine

TU Delft

Erasmus MC

ASSESSMENT OF RIGHT VENTRICLE MORPHOLOGY AND FUNCTION IN TETRALOGY OF FALLOT USING 3D ECHOARDIOGRAPHY

Using regional curvature and directionally decomposed ejection fraction

J.W. (Jop) Schneijdenberg

Student number : 4677471

13 Aug 2024

Thesis in partial fulfilment of the requirements for the joint degree of Master of Science in

Technical Medicine

Leiden University ; Delft University of Technology ; Erasmus University Rotterdam

Master thesis project (TM30004 ; 35 ECTS)
Thorax Biomedical Engineering, Dept. of Cardiology, Erasmus MC
29 Jan 2024 – 30 Aug 2024

Supervisors:
Dr. ir. J.G. (Hans) Bosch
Dr. A.E. (Annemien) van den Bosch

Thesis committee members:
Dr. ir. J.G. (Hans) Bosch, Erasmus MC (chair)
Dr. A.E. (Annemien) van den Bosch, Erasmus MC
Dr. B. (Beatrijs) Bartelds, Erasmus MC Sophia
Dr. ir. J. (Jouke) Dijkstra, LUMC

Universiteit Leiden

TU Delft Delft University of Technology

Erasmus University Rotterdam

Preface

Surgical and perioperative care for patients with congenital heart disease have improved significantly over the past decades. With high levels of patients now reaching adulthood, new challenges arise. The increasing adult population of congenital heart disease patients, now present themselves with severe morbidity in later life. Therefore, research in this patient population has added focus to the management of late onset morbidity, besides early paediatric intervention. The same trend is seen in research on patients with Tetralogy of Fallot, the most prevalent cyanotic congenital heart disease. This patient population faces high rates of right ventricular dysfunction, largely caused by leakage of their pulmonary valve. Surgical and percutaneous pulmonary valve replacement effectively remedies right ventricular dysfunction, but durability of artificial valves and re-intervention options are limited. Technological advancements in the field of cardiovascular imaging could be of great help in the optimisation of treatment timing in this patient population. In this thesis, the potential of using three-dimensional cardiac ultrasound will be investigated to enhance understanding of right ventricle pathophysiology in patients with Tetralogy of Fallot.

The Biomedical Engineering group of the Erasmus MC Cardiology department has over 50 years of experience in the field of cardiovascular imaging. Its multidisciplinary team focuses on investigating unprecedented imaging techniques to improve treatment of patients with cardiovascular disease. In close collaboration with clinicians from the Cardiology department, efficient development, validation, and implementation of novel techniques is achieved. The research performed during this thesis is a perfect example of an investigation that was only feasible due to the unique ecosystem present at Erasmus MC.

This thesis was performed to conclude my master's degree in Technical Medicine, with a track in Imaging & Intervention. With special interest in cardiology and an educational background on the leading edge of technology and healthcare, this project seamlessly merged my core interests into a clinically relevant master thesis project. The project challenged me to augment my technical skills in programming and geometry, and to transform research findings to clinical implications. I was encouraged to gain experience on an academic level, leading to the submission of an abstract to this year's EuroEcho-Imaging conference. Additionally, I got the opportunity to participate in patient care in different parts of the Cardiology department, giving me valuable insight in the highly specialised care provided at Erasmus MC.

Last seven months of work have led to this master thesis. The work consists of a medical paper highlighting the main findings obtained during this research, with in-depth technical elaborations on used techniques and calculations in the Supplements at the end of the manuscript.

Jop Schneijdenberg
Rotterdam, August 2024

Acknowledgements

I would like to start by thanking my supervisors Hans Bosch and Annemien van den Bosch for their guidance, patience, and critical appraisals of my work throughout the project. Hans, your in-depth knowledge of the subject, attention to detail, and willingness to dedicate time to me, have allowed me to grow on both a personal and academic level. Annemien, thank you for your insights, expertise, and adaptable mind-set throughout the project, as well as for introducing me to the clinical department. Your way of combining clinical work and highly innovative research was truly inspiring. Special thanks to Rory Zwaan for his daily supervision and approachability, and for being a perfect brainstorming partner for both my thesis and future career plans.

I would also like to express my gratitude to the scientific staff from the Biomedical Engineering department for their expertise and warm welcome. Especially Gerard van Burken for helping me if I had trouble with C++ and helping me organise my programming work. I would like to express my appreciation to the previous student, Yue Chen, for laying a strong foundation at the start of the project, which provided an excellent basis for further development. Big thanks to the cardiologists, A(N)IOS, sonographers, and VS/PAs from the Cardiology department for guiding me during clinical activities. Particularly Daniel Bowen, who both assisted in my research and allowed me to attempt my first cardiac ultrasound acquisitions.

Furthermore, I am thankful for the chats, coffee breaks, and lunches with the PhDs and post-docs at Rg4 and on the 23rd floor. Lastly, thanks to all friends and family who listened to my experiences and struggles, and for your advice throughout this project.

Contents

List of abbreviations

2D	Two-dimensional
3D	Three-dimensional
3DE	Three-dimensional echocardiography
ABD	Anterior boundary
AFW	Anterior free wall
AP	Anteroposterior
APX	Apex
CHD	Congenital heart disease
dEF	Decomposed ejection fraction
ECG	Electrocardiography
ED	End-diastolic
EDV	End-diastolic volume
EF	Ejection fraction
ES	End-systolic
ESV	End-systolic volume
IFW	Inferior free wall
IQR	Interquartile range
LFW	Lateral free wall
LT	Longitudinal
LV	Left ventricle
LVEF	Left ventricular ejection fraction
MC	Mean curvature
PAH	Pulmonary arterial hypertension
PBD	Posterior boundary
RBBB	Right bundle branch block
RD	Radial
rdEF	Regional decomposed ejection fraction
RV	Right ventricle
RVEF	Right ventricular ejection fraction
RVIT	Right ventricular inflow tract
RVOT	Right ventricular outflow tract
S’	Peak lateral tricuspid annular systolic velocity
SPB	Septal body
TAPSE	Tricuspid annular plane systolic excursion
ToF	Tetralogy of Fallot
TTE	Transthoracic echocardiogram
vcrMC	Volume corrected regional mean curvature
VSD	Ventricular septal defect

Assessment of Right Ventricle Morphology and Function in Tetralogy of Fallot using 3D Echocardiography

Using regional curvature and directionally decomposed ejection fraction

J.W. Schneijdenberg[a,b], R.R. Zwaan[b], A.E. van den Bosch[b], J.G. Bosch[b]

[a] *Educational program Technical Medicine; Leiden University Medical Center, Delft University of Technology & Erasmus University Medical Center Rotterdam.*
[b] *Department of Cardiology, Thorax Center, Erasmus Medical Center Rotterdam*

Abstract

Introduction: Tetralogy of Fallot (ToF) is a congenital heart disease requiring surgical correction in early childhood. Despite high surgical success rates, patients face severe morbidity during adulthood, primarily relating to the right ventricle (RV). Underlying pathophysiological processes remain largely unknown, but are commonly attributed to RV remodelling. Improved understanding of RV remodelling is essential for advancements in clinical decision making, requiring advanced monitoring techniques. Three-dimensional echocardiography (3DE) forms a promising option for the quantification of morphological and functional RV remodelling.

Aim: To identify global and regional differences in morphological and functional RV characteristics between ToF patients and healthy controls, using 3DE imaging. A software application will be developed to calculate global and regional mean curvature (MC) and directionally decomposed ejection fraction (dEF) to enhance understanding of RV remodelling in ToF patients.

Methods: Three-dimensional dynamic RV meshes were obtained from RV-focused 3DE studies of 50 ToF patients and 50 healthy controls, using commercially available software (TomTec 4D RV-Function). Regional morphological RV remodelling was assessed over nine regions using MC. Global and regional functional RV remodelling was evaluated over three regions using dEF in longitudinal (LT), radial (RD), and anteroposterior (AP) motion directions. A custom software application was developed for the calculation of both parameters, after which values were analysed and statistically compared within and between ToF patients and healthy controls. Correlations between dEF and left ventricular ejection fraction (LVEF) were investigated.

Results: RV remodelling was found to be a heterogeneous process, with different expressions throughout regions. Morphological RV remodelling was most evident in the posterior boundary, apex, and RV outflow tract regions, showing highly significant decreases of MC in ToF compared to healthy controls ($p<0.001$). Functional RV remodelling showed the most significant reduction of dEF in the AP motion direction in ToF patients compared to healthy controls ($p<0.001$), most evident in the anterior free wall region. The AP component of dEF was the only motion direction that did not show significant correlation with LVEF.

Conclusion: The posterior boundary, apex, and RV outflow tract regions showed largest decreases in curvature, making them highly interesting for further investigation. Deterioration of RV function was mostly assigned to decreased contribution of the AP wall motion direction to dEF, which showed no significant correlation with LVEF. Therefore, deterioration of the AP component of dEF was identified as a distinct feature of RV remodelling, making it an interesting candidate for advanced assessment of functional RV remodelling in ToF patients. Future research in ToF patients should focus on longitudinal follow-up, allowing for the identification of regions with significant remodelling over time. With the development of the software application, morphological and functional RV remodelling in any patient population can be investigated.

Keywords: Tetralogy of Fallot; Right Ventricle; Three-Dimensional Echocardiography

1. Introduction

1.1. Tetralogy of Fallot

Tetralogy of Fallot (ToF) is the most common cyanotic congenital heart disease (CHD) (1). Patients with ToF have an underdeveloped infundibular septum, leading to a combination of four cardiac features: a ventricular septal defect (VSD), right ventricle (RV) outflow tract obstruction, an overriding aorta, and RV hypertrophy (Figure 1A) (2, 3). In ToF patients, RV pressure is elevated to ensure adequate circulation to the lungs in the presence of the RV outflow tract obstruction. This increase in RV pressure results in RV hypertrophy and causes deoxygenated blood to shunt from the RV into the left ventricle (LV) through the VSD. This hemodynamic change leads to deoxygenation of the systemic circulation and cyanosis (4).

ToF patients require surgical repair in early childhood (5). During surgical correction of ToF, the VSD is closed with a patch, eliminating the shunt and redirecting LV flow towards the aorta. The RV outflow tract obstruction is relieved by RV muscle resection, and the pulmonary stenosis is addressed through valvotomy and transannular patching (Figure 1B) (6). Complete separation of systemic and pulmonary circulation is achieved as a result, restoring unobstructed flow to the aorta and pulmonary artery (7).

Even though surgical ToF repair manages to mimic physiological circulation, patients often face recurrent

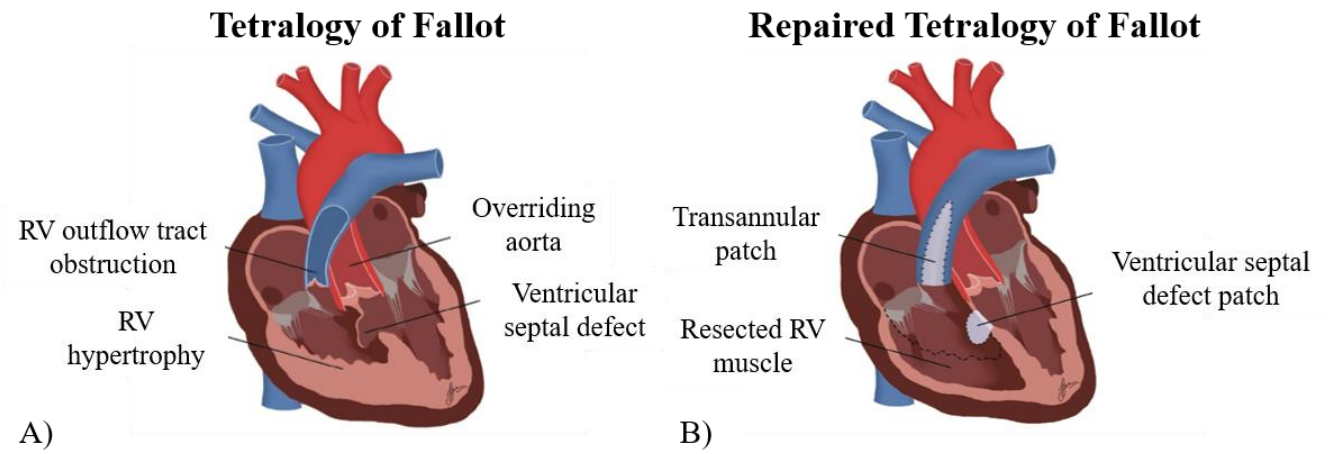

Figure 1: A) Heart showing four cardiac features associated with the congenital heart disease ToF, B) heart after surgical repair of ToF, showing three performed repairs. Adaptation from Tale et al. (8). RV: right ventricle.

hemodynamic issues as they progress into adulthood. A major cause of problems is related to pulmonary regurgitation as an iatrogenic effect of pulmonary stenosis relief as part of surgical ToF correction. Chronic pulmonary regurgitation leads to long standing RV volume overload, which eventually causes progressive RV dilatation and potentially RV dysfunction (5, 7). Adverse RV remodelling is associated with ventricular arrhythmias and sudden cardiac death in ToF patients. Cardiac conduction disorders and LV dysfunction have been identified as additional prognostic factors for the occurrence of adverse events in ToF patients (9, 10).

Adverse events as a result of RV dysfunction can be prevented by timely pulmonary valve replacement. Optimal timing of this intervention is of the essence. On the one hand, early valve replacement is encouraged as RV function fails to improve after pulmonary valve replacement if irreversible remodelling of RV function has already occurred (11). On the other hand, prosthetic pulmonary valves have limited durability and can only be replaced a limited number of times, advocating more conservative intervention (12, 13). However, the optimal criteria for pulmonary valve replacement in patients with repaired ToF remain uncertain (14).

For further optimization of pulmonary valve replacement timing, improved understanding of pathophysiological processes underlying changes in RV morphology and function is required. To achieve this, new monitoring techniques will have to be investigated for the quantification of RV remodelling in ToF patients (15, 16).

1.2. Echocardiography

Echocardiography is the most commonly used, first-line imaging modality for diagnosis and monitoring of patients with CHD. Its capabilities to assess cardiac morphology, physiology, pathophysiology, and function are essential for clinical management and prognosis of CHD patients (14, 17). Additional advantages of this technique include its non-invasive and real-time character, availability, and low cost (18).

In ToF patients, careful assessment of the RV is crucial. However, evaluating RV function and size using echocardiography is challenging due to its complex shape and anatomical location in the thorax. The RV has an asymmetrical crescent shape, making it impossible to rely on geometrical assumptions based on two-dimensional cross-sections. Additionally, RV function of ToF patients shows regional differences, making single two-dimensional measurements inadequate for the representation of RV function (17-19). Consequently, RV imaging must be performed by acquiring views from multiple angles to gain full insight in severity of disease. However, the RV is located directly behind the sternum, regularly causing artefacts in required imaging windows (18, 20, 21).

A potential solution may be found in the use of 3D echocardiography (3DE) for monitoring the RV in ToF patients. This imaging modality, with its ability to capture 3D images, eliminates the need for geometrical assumptions by visualising the entire RV in a single volume, allowing for regional quantifications (18, 22). Moreover, 3DE offers advantages over other cardiac imaging modalities, such as magnetic resonance imaging, due to its higher availability, lower cost, and shorter acquisition time (16, 23).

From 3DE studies, 3D endocardial surface models of the right ventricle can be obtained using commercially available semi-automatic segmentation tools (24, 25). Such tools provide 3D dynamic RV endocardial surface meshes that can be used for elaborate geometrical analyses of RV morphology and function by offline post-processing.

The analysis of 3DE based dynamic RV endocardial surface meshes is relatively new in cardiac imaging. Therefore, golden standard parameters for its use in geometrical RV analysis have not yet been established. Current applications mainly consist of volumetric measurements of end-diastolic volume (EDV) and end-systolic volume (ESV) for the calculation of ejection fraction (EF) (26). Though right

ventricular ejection fraction (RVEF) can be used to represent global systolic function of the ventricle, its dependency on load, interventricular mechanisms, and valve leakage presents challenges for its interpretation (18). Therefore, new regional parameters must be investigated to be able to improve current understanding of RV remodelling through the quantification of RV morphology and function (16).

1.3. 3DE parameters

A previous literature review identified regional curvature and directionally decomposed EF as promising parameters for the regional quantification of RV morphology and function (Appendix 1: Literature review). Curvature was selected as a valuable parameter for RV morphology, as it can be calculated over any segment of the RV surface, providing new insights on regional morphological changes in patients with ToF. Several studies have identified regional variations in morphological RV remodelling, revealing distinct patterns across different cardiac disorders (27-29).

Directionally decomposed EF was identified as a comprehensive parameter for 3DE based evaluation of global and regional RV function in patients with ToF. This parameter allows for quantification of ventricular contraction components along the three main anatomical axes of the RV. Previous publications using this parameter have shown that specific directions of wall motion are affected differently across various cardiac disorders (28, 30-32). Therefore, analysis of this parameter could yield in-depth insight in RV contraction patterns, enhancing the understanding of disease-specific functional RV remodelling.

1.4. Aim

The aim of this thesis is to identify global and regional differences in RV morphological and functional characteristics between ToF patients and healthy controls, using 3DE imaging. To achieve this, a software application will be developed to calculate RV curvature and directionally decomposed EF. This study will explore the global and regional differences of these parameters and their relation with cardiac electrical conduction and LV function, thereby enhancing our understanding of RV remodelling in ToF patients.

2. Methods

2.1. Study population and study design

A retrospective study was performed on 50 ToF patients and 50 healthy controls. Data of ToF patients who had undergone dynamic RV-focused 3DE examinations between January 2014 and March 2023 in our specialist CHD centre were extracted from a research database. A control group was composed of age- and gender-matched healthy volunteers who had undergone similar 3DE examination for research purposes. All 3D transthoracic echocardiograms (TTE) were reviewed by an experienced sonographer (DB), and those with moderate to good RV 3D image quality were considered for inclusion in this study.

2.2. 3D echocardiography

RV-focused full volume 3DE studies were taken from an apical window. Studies were performed during breath hold, using a Philips ultrasound system (EPIQ7, X5-1 matrix array transducer, Philips Healthcare, Best, The Netherlands). Recordings were either four to six beat full volume acquisitions, or made with single beat HeartModel software (Philips Healthcare). Offline semi-automatic segmentation of dynamic 3DE data was performed using commercially available software (4D RV-Function 2.0, TomTec Imaging GmbH, Unterschleissheim, Germany). Contours were checked and manually adjusted by an experienced sonographer (DB) if necessary. Output consisted of 3D dynamic RV surface renderings, commonly referred to as 'beutels'. Beutels were exported from TomTec as a set of RV triangulated mesh files, one per frame of the dynamic 3DE study. The number of files in a set varied per patient, depending on heart rate and frame rate of the acquisition.

2.3. 3D RV analysis

A software application for beutel analysis (RV-Dynamics) was previously developed in-house in C++ (33). RV-Dynamics was adapted and extended with additional functionalities for RV morphology and RV function quantification as part of this thesis. For each patient, a complete set of RV triangulated mesh files was loaded into the application for analysis.

2.3.1. RV morphology

RV morphology was quantified by the calculation of mean curvature (MC). Curvature is defined as the inverse of the radius of the circle osculating the curve of a surface. An osculating circle is a circle touching the curve, such that the circle and curve touch without crossing. Hereby, the curvature can be represented by the radius of the circle. MC quantifies average curvature at a specific point on a 3D surface, by averaging curvature of the surface in multiple angles of intersection perpendicular to the surface (34). Negative MC signifies a locally concave surface, zero MC a flat surface, and positive MC a convex surface which is assessed from a viewpoint outside the beutel (Figure 2). MC was computed in accordance with calculations in the article of Meyer et al. (35), for each vertex separately in end-systolic (ES) and end-diastolic (ED) frames (Supplement S.1 Curvature). The ED frame was defined as the frame with largest RV volume and the ES frame was defined as the frame with smallest RV volume (36).

ToF patients are known to develop RV dilatation as a result of volume overload, leading to overall reduction of curvature (15). Volume correction was performed to compensate for RV dilatation effects, allowing for more precise quantification of morphological RV remodelling. An adaptation of the method proposed by Addetia et al. (27) was applied. MC were divided by a normalisation term for volume correction. The normalisation term corresponded to the curvature of a sphere, having the same volume as the RV of the patient. For ED MC, volume correction was performed using EDV. For ES MC, volume correction

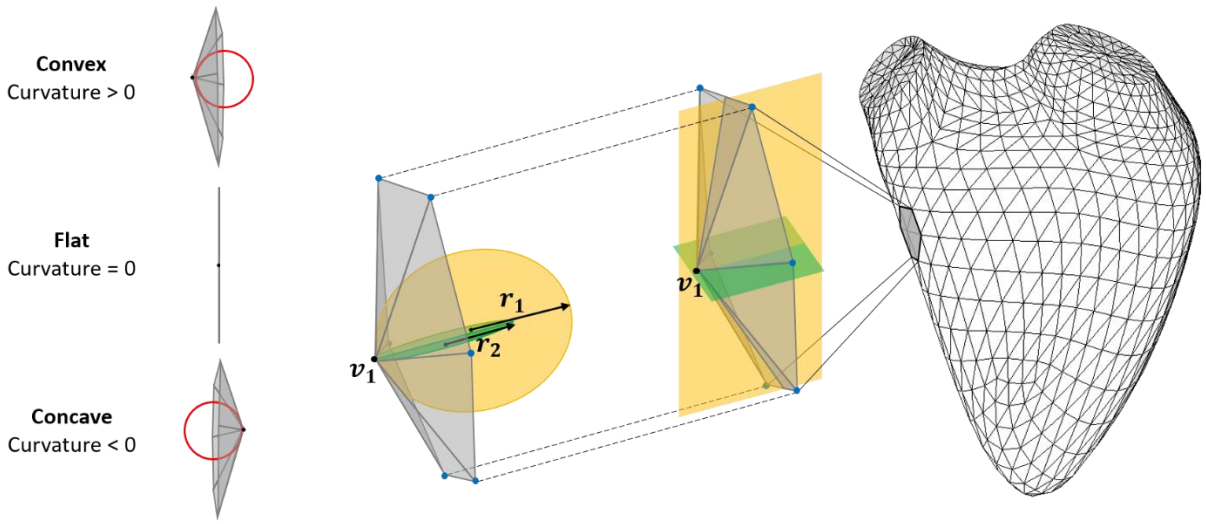

Figure 2: Demonstration of mean curvature calculation for vertex v_1, quantified in multiple planes (yellow and green) as the inverse of the radius (r_1 and r_2) of circles osculating the surface between all neighbouring vertices (blue). Convex surfaces result in positive, flat surfaces in zero, and concave surfaces in negative mean curvature values.

was performed using ESV. As a result, ED and ES volume corrected MC values were generated, expressed as a percentage of the curvature of above-mentioned sphere (Supplement S.1.5 Volume correction).

For regional MC calculation, eleven different regions were defined based on literature and expert opinion (28, 37, 38). This subdivision aimed to enable detailed assessment of regional remodelling effects of the RV, by quantifying specific morphological features. Regions comprised the RV inflow tract (RVIT), RV outflow tract (RVOT), infundibulum, anterior free wall (AFW), inferior free wall (IFW), lateral free wall (LFW), septum, septal body (SPB), anterior boundary (ABD), posterior boundary (PBD), and apex (APX) (Figure 3). Vertices were each assigned to one of these regions, after which the regional average was determined for the calculation of regional MC (Supplement S.1.6 Region definition). The SPB region contains a selection of vertices located on the RV septum, representing most explicit curvature of the septum. The infundibulum region was not analysed due to its complex saddle shape which cannot be meaningfully assessed using MC as a parameter. Regional MC calculations were performed in ED and ES for all regions, except the infundibulum and septum. Volume correction of regional MC values was performed using partial EDV and ESV. These volumes were spanned between the regional endocardial surface and the ED or ES centre of mass respectively, resulting in volume corrected regional mean curvature (vcrMC) values.

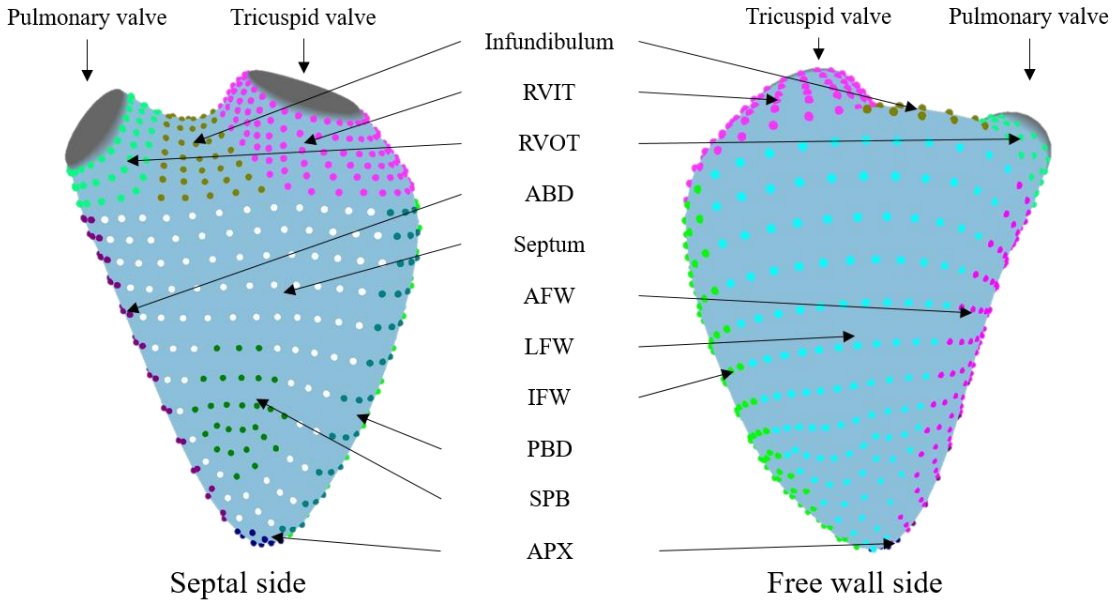

Figure 3: Regional division of vertices on the endocardial surface for regional mean curvature calculation. RVIT: right ventricular inflow tract; RVOT: right ventricular outflow tract; ABD: anterior boundary; AFW: anterior free wall; LFW: lateral free wall; IFW: inferior free wall; PBD: posterior boundary; SPB: septal body; APX: apex.

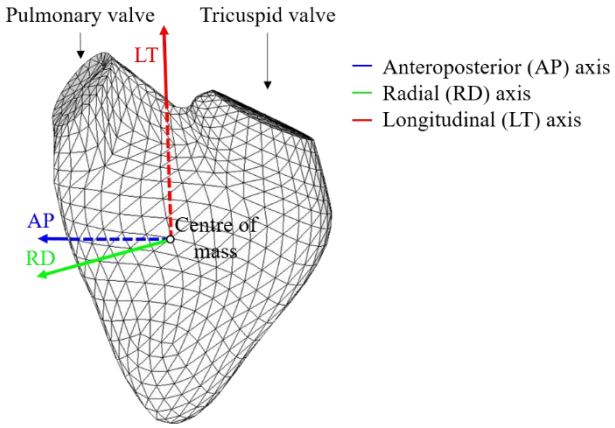

Figure 4: Axis definition and beutel orientation seen from a septal view. Anteroposterior (blue), radial (green) and longitudinal (red) axes originating from the RV centre of mass in the end-systolic frame.

Regional differences in curvature were visualised by projecting a heat map over the beutel of an individual patient, colour-coding vertices depending on their volume corrected MC value (Supplement S.1.7 Visualisation).

2.3.2. RV function

Detailed quantification of RV function was achieved through the decomposition of RV contraction into three orthogonal anatomical directions. RV wall motion was decomposed in anteroposterior (AP), radial (RD), and longitudinal (LT) direction, in line with literature findings (39, 40).

To ensure consistent axis definition for all patients, standardised orientation and alignment of all meshes was performed before analysis. A new coordinate system was defined with axes in AP, RD, and LT direction, corresponding to the x-, y-, and z-axis respectively. The origin of the coordinate system was located on the RV centre of mass in the ES frame (Figure 4) (Supplement S.2.1 Axis definition).

Accordingly, wall motion of RV meshes was decomposed into AP, RD, and LT direction components conforming to the newly defined axes. For the computation of directional components of wall motion, either the x-, y-, or z-coordinate of all vertices was allowed to change whilst keeping the other two coordinates constant on their ED value. As a result, three sets of directionally decomposed meshes were created, each allowing for the quantification of wall motion in either the AP, RD, or LT direction (Figure 5).

From these meshes, decomposed EF (dEF) could be calculated in AP, RD, and LT direction as a measure for directional RV function. EF is defined as the ratio between stroke volume and EDV. Stroke volume is calculated by subtraction of ESV from EDV (Formula 1). By using ESV calculated from decomposed meshes, EF brought about by wall motion in one specific direction can be quantified (Supplement S.2.2 Mesh decomposition).

$$EF = \frac{EDV - ESV}{EDV} \quad (1)$$

To study ratios between the three dEF components, relative decomposed EF (rdEF) was determined. Each dEF value was divided by the sum of all three dEF values. As a result, changes in contribution of each dEF component to global EF could be studied, independent of overall RV function (Supplement S.2.3 Relative decomposed EF).

For regional assessment of dEF and rdEF, four different regions were defined based on literature and expert opinion (38, 41). This subdivision aimed to enable detailed assessment of regional RV function, and to quantify differences between regions. The subdivision contained fewer and larger regions than the division used for regional MC calculations. Regions comprised the AFW, IFW, LFW, and septum (Figure 6). Vertices were each assigned to one of these regions, forming a regional surface on the RV mesh. Regional dEF and rdEF were computed by calculating partial EDV and ESV spanned between the regional endocardial surface and ES centre of mass, using Formula 1. Regional function of the septum was not included in analysis, as decomposed motion did not prove meaningful in that region (Supplement S.2.4 Region definition).

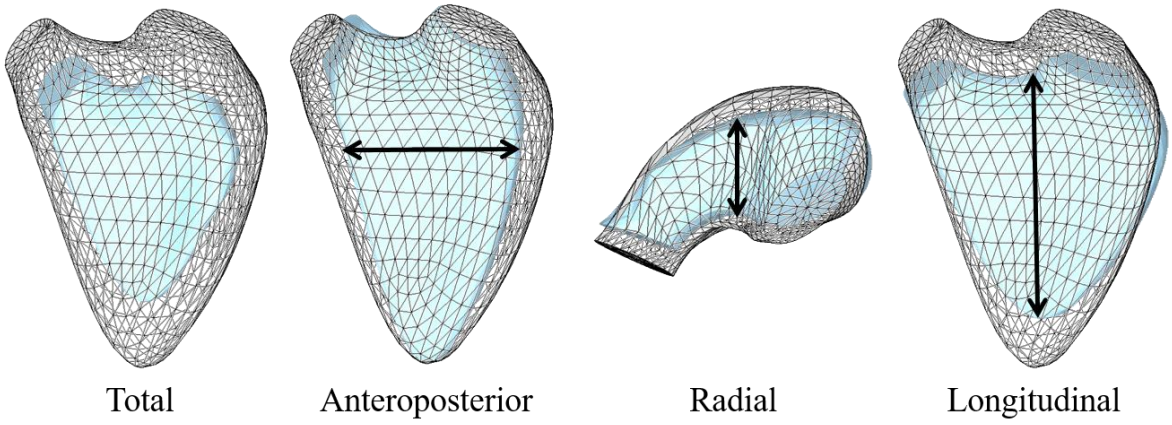

Figure 5: Demonstration of total wall motion and decomposed wall motion in anteroposterior, radial, and longitudinal direction, showing end-diastolic volumes (black meshes) and end-systolic volumes (blue beutels).

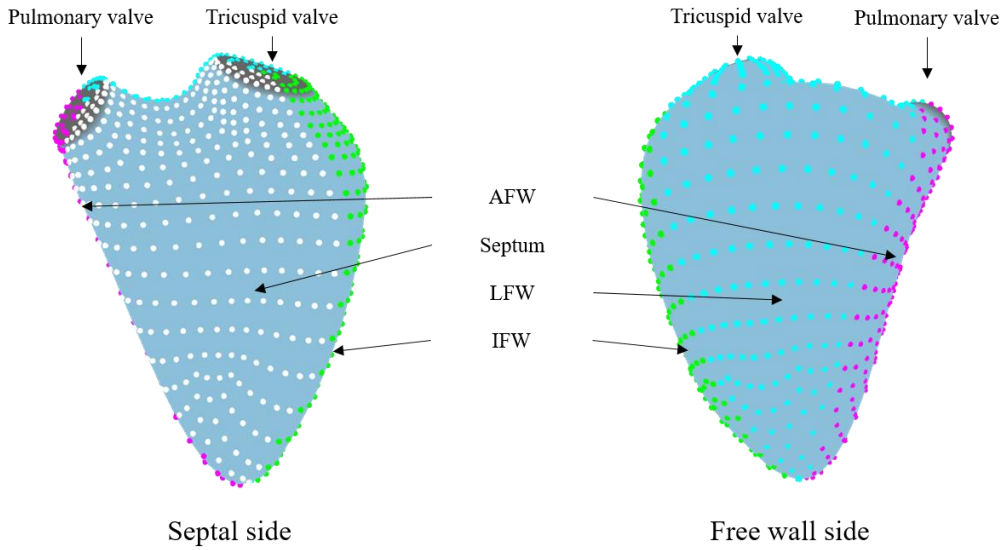

Figure 6: Regional division of vertices on the endocardial surface for regional dEF and rdEF calculation. AFW: anterior free wall; LFW: lateral free wall; IFW: inferior free wall.

2.4. Relation with cardiac electrical conduction and LV function

The correlation of vcrMC, dEF, and rdEF with the electrocardiogram (ECG) characteristics QRS-duration, heart axis, and the presence of a RBBB in ToF patients was calculated to investigate the influence of RV remodelling on electrical conductivity of the heart.

The correlation of dEF and rdEF with echocardiography derived left ventricular ejection fraction (LVEF) was investigated in the ToF population to assess the relation between RV function and LV function.

2.5. Statistical analysis

Data distributions were examined through histograms and the Shapiro-Wilk normality test. Normally distributed, continuous variables were expressed as mean ± standard deviation and compared using a Student's *t*-test. Non-parametric variables were presented as median and interquartile ranges (IQR) and compared using a Mann-Whitney U test. Pearson's and Spearman's coefficients were calculated for correlation assessment of parameters with normal and non-normal distribution respectively. RV morphology and function parameters were all considered as non-parametric variables to allow for interregional comparison. A p-value below 0.05 was considered significant. Statistical analysis was performed in SPSS for Windows (Version 28.0, SPSS Inc., Chicago, IL, USA).

3. Results

3.1. Baseline characteristics

Baseline characteristics of the study population are shown in Table 1. RV EDV was significantly higher in ToF patients in comparison to healthy controls ($p<0.001$). Additionally, ToF patients showed significant reduction in RVEF ($p<0.001$) and LVEF ($p<0.001$) compared to healthy controls.

3.2. RV morphology in ToF

Calculated vcrMC values are shown in Table 2. Differences between ToF and healthy controls appeared to be larger in ES than in ED. Largest decreases in vcrMC were found in the PBD, APX, and RVOT regions in both ED and ES ($p<0.001$), signifying a bulging and less convex regional morphology in ToF patients compared to healthy controls.

Despite reduction in both ED and ES, the PBD did show a marked increase in vcrMC from ED to ES. The SPB region was the only RV region that showed concavity throughout the cardiac cycle in both populations. SPB vcrMC values were less negative in ToF, representing septal flattening compared to the more concave interventricular septa in healthy controls.

An increase in vcrMC, rather than a decrease, could only be seen in the IFW region in ToF patients compared to healthy controls. The AFW and LFW regions of the free wall showed slightly decreased vcrMC. The ABD region was the only region showing no significant difference in ToF patients in both ED ($p=0.054$) and ES ($p=0.074$).

Regional MC calculations showed significant differences between ToF and healthy controls over all regions before volume correction. Larger differences between ED and ES values of regional MC were seen in healthy controls than in ToF patients, suggesting more dynamic contraction in healthy controls (Supplement S.3 Supplementary results, Table S3).

An illustrative case of one ToF patient and one healthy control is shown in Figure 7, allowing qualitative comparison between both groups. Decreased convexity can be seen in the PBD, APX, and RVOT regions comparing the ToF patient beutel with the healthy control beutel. Increased convexity is shown in the IFW, and decreased concavity is visualised in the SPB. Maintained vcrMC can be seen in the ABD and AFW regions.

Table 1: Baseline characteristics.

Variable	ToF (n=50)	Controls (n=50)	p-value
Age, years	38 [22 - 46]	34 [25 - 47]	0.717
Female, n (%)	18 (36)	18 (36)	
BMI, kg/m^2	23.4 ± 2.9	23.6 ± 3.1	0.697
BSA, m^2	1.9 ± 0.2	1.9 ± 0.2	0.289
RV EDVi, mL/m^2	95 [77 - 120]	61 [50 - 70]	<0.001
RVEF, %	45 ± 7	57 ± 4	<0.001
LVEF, %	54 [50 - 58]	63 [58 - 66]	<0.001
Surgical interventions			
Transannular patch, n (%)	23 (46)		
Pulmonary valve re-intervention, n (%)	27 (54)		
Severe pulmonary regurgitation, n (%)	5 (10)		
Severe pulmonary stenosis, n (%)	19 (38)		
Severe tricuspid regurgitation, n (%)	3 (6)		
ECG			
Sinus rhythm, n (%)	47 (94)		
QRS-duration, s	135 [114 – 161]		
Heart-axis, °	42 ± 68		
RBBB, n (%)	40 (80)		
Paced, n (%)	2 (4)		

Values are presented as mean ± standard deviation or median [interquartile range]. ToF: Tetralogy of Fallot; BMI: body mass index; BSA: body surface area; RV EDVi: right ventricular end-diastolic volume indexed to BSA; RVEF: right ventricular ejection fraction; LVEF: left ventricular ejection fraction; ECG: electrocardiogram; RBBB: right bundle branch block.

Table 2: End-diastolic and end-systolic volume-corrected regional mean curvature in ToF and healthy controls.

	End-diastolic			End-systolic		
Region	ToF (n=50)	Controls (n=50)	p-value	ToF (n=50)	Controls (n=50)	p-value
Global	106 [102 - 108]	112 [108 - 116]	<0.001	105 [99 - 110]	116 [112 - 125]	<0.001
Free wall	81 [80 - 86]	84 [78 - 90]	0.352	76 [72 - 81]	80 [74 - 93]	0.027
AFW	56 [50 - 68]	70 [55 - 83]	0.014	47 [41 - 59]	53 [43 - 73]	0.188
LFW	79 [71 - 85]	81 [74 - 87]	0.448	76 [66 - 86]	86 [74 - 104]	0.004
IFW	110 [101 - 116]	102 [96 - 112]	0.029	104 [93 - 113]	95 [84 - 103]	0.012
ABD	539 [484 - 593]	492 [441 - 578]	0.054	554 [490 - 607]	497 [439 - 587]	0.074
PBD	262 [243 - 288]	294 [264 - 329]	<0.001	303 [255 - 330]	371 [322 - 426]	<0.001
APX	481 [448 - 531]	554 [486 - 619]	<0.001	439 [386 - 479]	547 [467 - 669]	<0.001
SPB	-50 [-62 - -42]	-64 [-83 - -52]	0.001	-48 [-58 - -38]	-62 [-77 - -52]	<0.001
RVIT	100 [90 - 109]	107 [98 - 122]	0.003	100 [85 - 107]	115 [94 - 130]	0.001
RVOT	109 [96 - 125]	131 [115 - 141]	<0.001	108 [88 - 122]	129 [114 - 140]	<0.001

Values are presented as percentages, median [interquartile range]. ToF: Tetralogy of Fallot; AFW: anterior free wall; LFW: lateral free wall; IFW: inferior free wall; ABD: anterior boundary; PBD: posterior boundary: APX: apex; SPB: septal body; RVIT: right ventricular inflow tract; RVOT: right ventricular outflow tract.

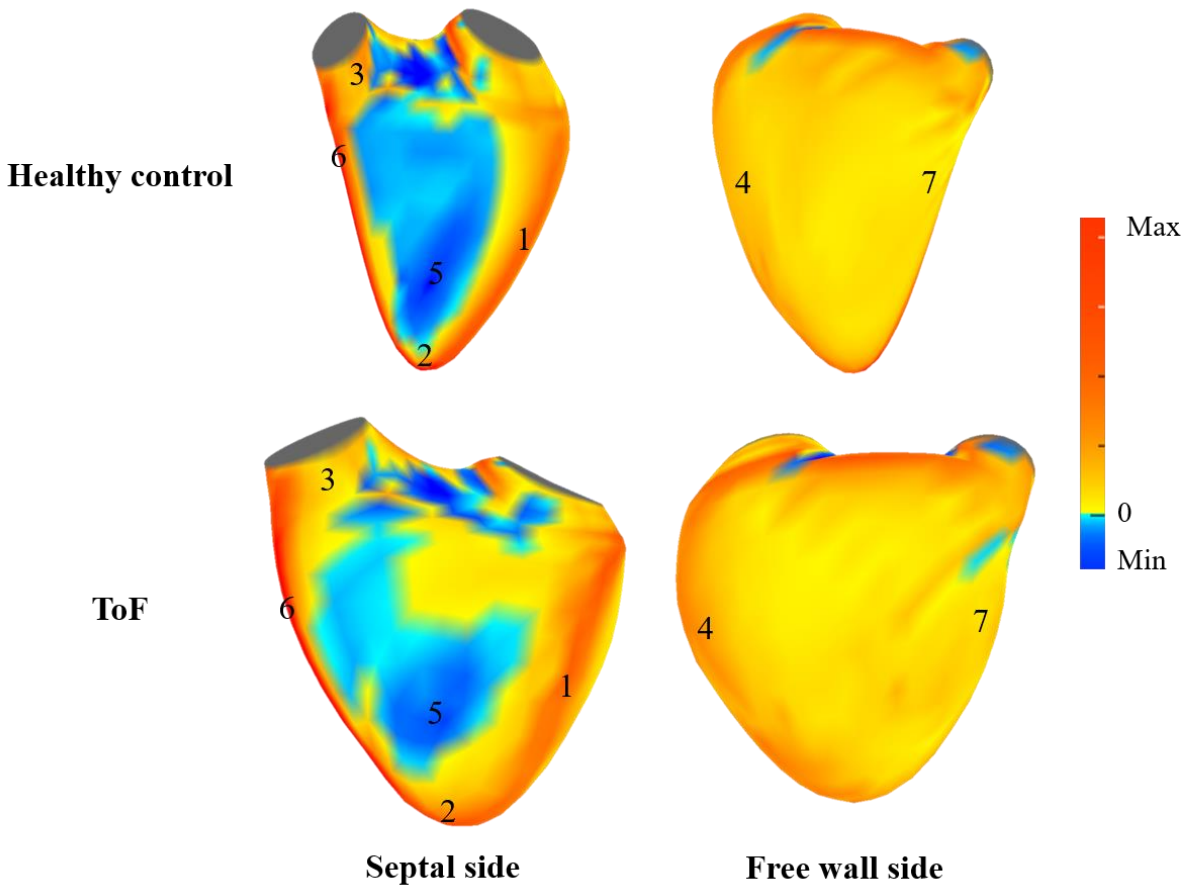

Figure 7: Illustration of volume corrected mean curvature values of a representative ToF patient and a healthy control in end-diastole, showing the septal and free wall side of the RV beutel. Decreased convexity is seen in ToF versus healthy controls in the (1) posterior boundary, (2) apex, and (3) right ventricular outflow tract. Increased convexity is shown in the (4) inferior free wall. Decreased concavity is visualised in the (5) septal body. Maintained volume corrected mean curvature can be seen in the (6) anterior boundary and (7) anterior free wall. ToF: Tetralogy of Fallot; Max: maximum volume corrected mean curvature value; Min: minimum volume corrected mean curvature value.

3.3. RV function in ToF

Decomposition of RV wall motion for the calculation of dEF revealed significant reduction in EF over all decomposition directions, comparing ToF patients to healthy controls (p<0.001). Largest reduction in dEF was found in the AP direction, followed by the RD and LT direction respectively (Table 3).

Relative changes in directional contributions identified the AP component of RV wall motion as the largest contributor to RVEF in both ToF patients (38% [31 - 42]) and healthy controls (40% [37 - 44]). rdEF in AP direction was slightly, but significantly, reduced in ToF patients compared to healthy controls (p=0.004). On the contrary, a significant increase (p=0.009) of rdEF in longitudinal direction was found in ToF patients (28% [26 - 33]) compared to healthy controls (26% [23 - 31]) (Table 3). Decrease of rdEF in AP direction and complementary increase of rdEF in LT direction signifies more severe deterioration of dEF in AP direction than in LT direction in patients with ToF. The RD component of rdEF showed no significant change between both populations (Figure 8) (Appendix 2: Abstract EuroEcho).

Table 3: Decomposed and relative decomposed RV ejection fraction in ToF and healthy controls.

	Decomposed EF			Relative decomposed EF		
Direction	ToF (n=50)	Controls (n=50)	p-value	ToF (n=50)	Controls (n=50)	p-value
Anteroposterior	21 [17 - 24]	31 [26 - 35]	<0.001	38 [31 - 42]	40 [37 - 44]	0.004
Radial	19 [15 - 23]	24 [22 - 30]	<0.001	33 [29 - 39]	32 [29 - 38]	0.649
Longitudinal	16 [14 - 18]	20 [17 - 24]	<0.001	28 [26 - 33]	26 [23 - 31]	0.009

Values are presented as percentages, median [interquartile range]. EF: ejection fraction; ToF: Tetralogy of Fallot.

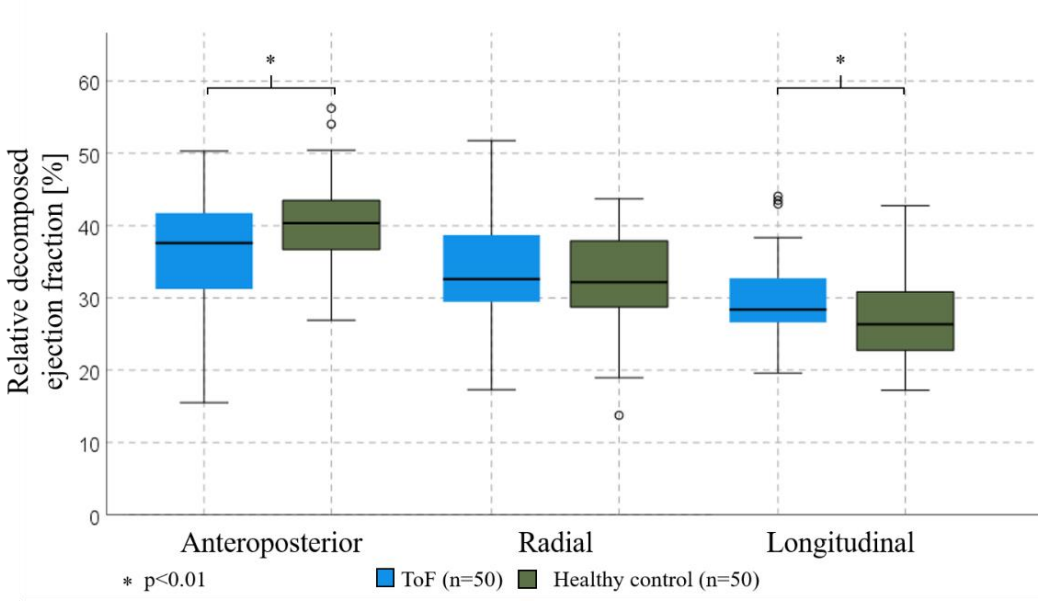

Figure 8: Comparison of relative decomposed RV ejection fraction in anteroposterior, radial, and longitudinal directions between ToF patients and healthy controls. ToF: Tetralogy of Fallot.

Regional assessment of dEF identified the LFW as the region with highest regional EF in healthy controls, followed by the IFW and AFW respectively (Table 4). In all three regions, each direction of decomposed EF was significantly decreased except for the component in LT direction in the AFW. Additionally, the AFW showed a comparable pattern in dEF and similar pattern in rdEF as the global RV. In this region, a significant decrease of rdEF in AP direction was found in ToF patients (36% [28 - 44]) compared to healthy controls (44% [37 - 53]). An increase was seen for rdEF in LT direction with 32% [28 - 37] in ToF, compared to 26% [22 - 30] in healthy controls. Changes in rdEF were less evident in other RV regions.

3.4. Correlation of LVEF with RV function

A significant correlation of 0.412 was found between dEF in the RD direction and LVEF (p=0.003). dEF in the LT direction also showed a significant correlation of 0.455 with LVEF (p<0.001). These correlations signify a positive coupling of RV dEF in RD and LT direction to LVEF. The AP component of dEF did not show significant correlation with LVEF (Figure 9). rdEF in AP, RD, and LT direction did not show significant correlation with LVEF.

Table 4: Regional decomposed and regional relative decomposed RV ejection fraction in ToF and healthy controls.

		Decomposed EF			Relative decomposed EF		
Region	Direction	ToF (n=50)	Controls (n=50)	p-value	ToF (n=50)	Controls (n=50)	p-value
AFW	Total	37 [32 - 45]	50 [46 - 55]	<0.001			
	Anteroposterior	20 [14 - 24]	31 [24 - 37]	<0.001	36 [28 - 44]	44 [37 - 53]	<0.001
	Radial	16 [11 - 20]	21 [16 - 25]	0.006	33 [23 - 37]	31 [23 - 35]	0.356
	Longitudinal	16 [15 - 19]	18 [14 - 21]	0.273	32 [28 - 37]	26 [22 - 30]	<0.001
LFW	Total	46 [42 - 52]	65 [62 - 68]	<0.001			
	Anteroposterior	21 [17 - 25]	32 [28 - 37]	<0.001	38 [35 - 42]	39 [36 - 46]	0.101
	Radial	19 [15 - 22]	26 [21 - 32]	<0.001	34 [28 - 38]	33 [27 - 40]	0.852
	Longitudinal	16 [14 - 19]	21 [18 - 25]	<0.001	29 [25 - 33]	26 [23 - 31]	0.086
IFW	Total	52 [47 - 57]	64 [62 - 66]	<0.001			
	Anteroposterior	21 [17 - 25]	28 [25 - 32]	<0.001	35 [32 - 43]	39 [35 - 44]	0.046
	Radial	20 [16 - 24]	23 [19 - 28]	0.003	33 [28 - 37]	31 [28 - 38]	0.210
	Longitudinal	17 [15 - 20]	21 [19 - 25]	<0.001	28 [27 - 34]	30 [24 - 34]	0.482

Values are presented as percentages, median [interquartile range]. EF: ejection fraction; ToF: Tetralogy of Fallot; AFW: anterior free wall; LFW: lateral free wall; IFW: inferior free wall.

Table 5: Correlation between LV ejection fraction and decomposed and relative decomposed RV ejection fraction in patients with ToF.

	Decomposed EF		Relative decomposed EF	
Direction	Correlation coefficient	p-value	Correlation coefficient	p-value
Anteroposterior	0.272	0.056	-0.156	0.281
Radial	0.412	0.003	0.178	0.216
Longitudinal	0.455	<0.001	0.029	0.840

Values are presented as Spearman's coefficients. EF: ejection fraction; ToF: Tetralogy of Fallot.

3.5. Correlation of ECG characteristics with RV morphology and function

The investigation of correlations between the computed parameters for RV morphology and function and ECG characteristics did not yield any significant results.

4. Discussion

A software application was developed for the quantification of global and regional RV morphology and function using 3DE imaging. This application allowed for the objective assessment of vcrMC and dEF of the RV, demonstrating the ability to differentiate between ToF patients and healthy controls. The PBD, APX, and RVOT regions were identified as key regions contributing to morphological RV remodelling in ToF patients. Functional RV remodelling was best observed in the AFW region. The AP component of dEF proved to be the largest contributor to RVEF, and also showed the largest reduction in ToF patients compared to healthy controls. This component did not show significant correlation with LVEF, whereas dEF in RD and LT direction did show a significant correlation.

Additionally, larger differences in curvature between ToF and healthy controls were observed in ES than in ED. The PBD, APX, and RVOT regions exhibited the most notable decreases in convexity, while the SPB region showed a decreased concavity in ToF. In contrast, the morphology of the ABD and AFW regions remained similar between ToF and healthy controls, but RV function showed the most changes in the AFW region. No significant correlation of vcrMC and dEF with cardiac electrical conduction characteristics was identified.

This study demonstrated that RV remodelling is a heterogeneous process across different regions, enhancing our understanding of RV remodelling in ToF patients. To the author's knowledge, no study of this size has yet been performed.

4.1. Implications of morphological RV remodelling

A wide variety in regional MC changes between ToF patients and healthy controls was observed across different regions of the RV. This finding is consistent with other published studies which also report significant diversity in morphological changes between RV regions (28, 42).

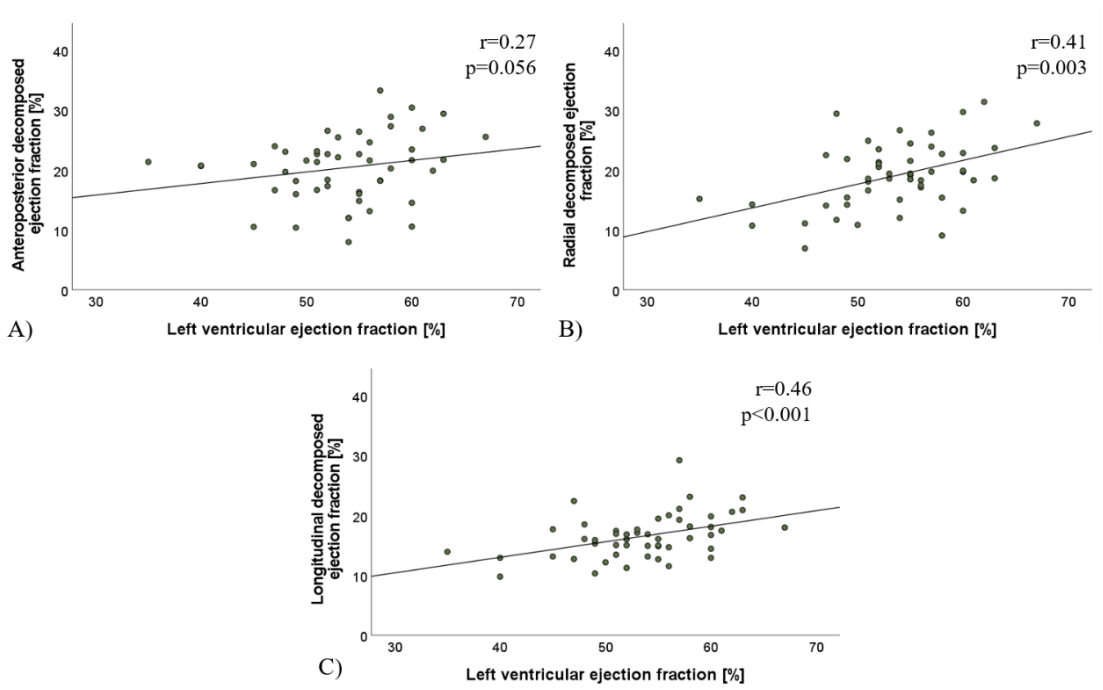

Figure 9: Scatterplots showing correlations between LV ejection fraction and decomposed RV ejection fraction in A) anteroposterior, B) radial, and C) longitudinal direction. Spearman's correlation coefficients (r) were calculated.

The PBD region of the RV in ToF patients was identified as one of the regions with the most significant decrease in convexity compared to healthy controls. Despite its flattening in ED, this region showed a large increase in curvature between ED and ES. Therefore, this region reflects behaviour that has also been observed in other studies, where RV presents preserved function despite dilatation (43). Another region that showed highly significant curvature changes in ToF patients was the APX. This change corresponds with the extensively investigated apical flattening observed in ToF patients (28, 42, 44, 45). The specific flattening of the apex may be attributed to anatomical variation in the myofiber structure in the RV of ToF patients, as reported by Sanchez-Quintana et al. (46). Calculation of vcrMC could be a good parameter to assess apical flattening in patients with ToF. Additionally, RVOT curvature showed significant differences between ToF and healthy controls. The RVOT region is particularly affected in ToF patients, since RVOT obstruction relief is a major part of surgical correction. The decreased curvature in this region, compared to healthy controls, may result from the valvulotomy and the use of a transannular patch to alleviate RVOT obstruction (47). Besides flattening of convex regions of the RV, the SPB region showed a decrease in concavity in ToF patients compared to healthy controls. Septal flattening is a well-known phenomenon in volume overloaded RV (48, 49). Two studies on RV curvature have even reported a change from concavity to convexity in case of pressure and volume overload of the RV (27, 28). However, convexity was not observed in this population of ToF patients. This discrepancy could be due to the different regional definitions used in this research compared to earlier publications. Additionally, baseline differences in cardiac function between the population in this study and those in previous research could contribute to the differing findings.

Whereas most curvatures moved towards zero in ToF patients, there was higher curvature in the IFW. The IFW was the only region showing increased convexity in ToF patients compared to healthy controls. This phenomenon has been identified before in ToF patients as basal bulging (42). The cause of basal bulging has not yet been identified, but a role in the occurrence of tricuspid regurgitation has been suggested (45).

Addetia et al. also investigated regional curvature, but in patients with pulmonary arterial hypertension (PAH) instead of ToF patients. They observed smaller curvature differences between ED and ES in PAH patients than in healthy controls, which was attributed to a loss of dynamic changes during the cardiac cycle in PAH patients (27). Similar changes were seen during this study, where differences between ED and ES in regional MC values before volume correction were smaller in ToF patients than in healthy controls. These observations completely disappeared after volume correction, and were therefore attributed to dilatation effects seen in ToF patients. This difference observed between ToF patients and PAH patients could be regarded as a difference between volume and pressure overloaded RV, as suggested in an earlier study (28). An observation that has not been reported in earlier studies, is the larger differences in curvature present in ES compared to ED in both ToF patients and healthy controls. This finding may provide a new perspective on current parameters for the assessment of the RV. Measurements of RV dimensions are mostly performed in the ED frame, in accordance with guidelines (18). Measurement of these parameters in ES may provide new insights and result in better discriminative power.

4.2. Implications of functional RV remodelling

The investigation of wall motion in various anatomical directions provided insights into the heterogeneity of functional RV remodelling. It was found that EF resulting from wall motion in the AP direction was the largest contributor to RVEF in both ToF patients and healthy controls. Conversely, dEF in the LT direction was identified as the smallest contributor to RVEF. This result contrasts with findings of Bidviene et al., who reported that dEF in the LT direction was the largest contributor and dEF in the AP direction was the smallest contributor to RVEF (28, 30). The population in the studies of Bidviene et al. was notably younger and mostly female, with more severe RV degradation due to increased dilatation and a high percentage of transannular patch use. Differences found in contributions of the AP and LT components to RVEF in this study may reflect varying patterns of RV remodelling at different stages of the disease.

From the results of this investigation, the effectiveness of functional ultrasound parameters can be disputed. Currently recommended functional parameters for the quantification of RV function, such as tricuspid annular plane systolic excursion (TAPSE), peak lateral tricuspid annular systolic velocity (S') and Doppler tissue imaging, solely quantify longitudinal RV contraction (17-19). However, from the results of this research, it can be concluded that dEF in LT direction shows least deterioration in ToF patients when compared to the RD and AP components of dEF. Assessment of RV function through the decomposition of EF in three anatomical directions could lead to new insights, allowing for more detailed identification of functional remodelling, potentially in an earlier stage of disease.

While the LT component of dEF showed the least deterioration in ToF patients compared to healthy controls, the AP component showed the most deterioration. Analysis of the correlation between dEF and LVEF revealed that the AP component of dEF did not correlate significantly with LVEF, in contrast with the RD and LT component. This suggests that the deterioration of dEF in the AP direction is a distinct feature of RV remodelling. Consequently, this RV characteristic may not be effectively quantified by LVEF, making the AP component of dEF a valuable measure for assessing advanced functional RV remodelling in ToF patients. Further research is needed to evaluate its clinical significance.

Regional assessment of dEF indicates that the AFW of the RV may play a crucial role in the functional remodelling of the RV. Patterns observed in rdEF in the global RV were similar to the patterns observed in the AFW. This pattern consisted of a significant decrease of rdEF of the AP component, a significant increase of the LT component and preserved rdEF of the RD component. These findings suggest that the AFW could be a region of interest for research after functional remodelling of the RV in patients with ToF. The AFW region is located directly below the pulmonary valve and is part of the RVOT. Earlier research already identified remarkable anatomical changes in the AFW region in patients with ToF compared to healthy individuals, which could be an explanation for the found pattern (46). Regional differences in RV function, especially surrounding the RVOT, have been associated with functional impairment in patients with ToF underlining the importance of regional RV function assessment (50, 51).

4.3. Lack of correlation with ECG characteristics

This study did not manage to correlate ECG characteristics with vcrMC, dEF, or rdEF. Correlations with QRS-duration, heart axis, and the presence of an RBBB were investigated, but neither showed significant results. However, electrical conduction characteristics have been correlated with RV morphology and function in an earlier study (52). A potential cause for not finding correlations between ECG characteristics and vcrMC could be the investigation of linear correlation only and lack of covariate adjustment. Bitterman et al. found nonlinear associations between QRS-duration and RVEF, EDV and ESV in patients with ToF, after covariate adjustment. Additionally, time independent variables were used for the definition of electromechanical dyssynchrony by looking at QRS-duration, delay between septal and lateral peak strain, and the presence of septal flash (52). Investigating covariate-adjusted nonlinear correlation and different electromechanical dyssynchrony characteristics could have enabled the identification of significant correlations.

4.4. Limitations

Limitations faced in this research were partly inherent to the imaging technique used. Due to the anatomical position of the RV in the thorax, lung and bone tissue regularly cause shadowing of specific RV regions. The AFW and ABD region are especially susceptible to shadowing as a result of their position directly behind the sternum (53). High quality ultrasound equipment and highly skilled sonographers are essential for successful 3DE acquisition. Only 3DE studies of good quality were considered for inclusion in this research. Therefore, analyses performed in this study may not be applicable to all ToF patients. Additionally, imaging quality of anterior regions may have been lower and segmentations less accurate than other regions, with a potential effect on outcomes.

Dynamic surface meshes were obtained using a semiautomatic segmentation software application. This software application required manual interactions and fine tuning for optimization of RV meshes. As a result of these manual steps, segmentation was sensitive to operator dependent variations. Earlier research showed reasonable intra- and interobserver variability in the segmentation process of TomTec 4D RV-Function (37). However, a certain degree of inaccuracy as a result of these manual steps is inevitable. Inaccuracies could be minimised through automation or further standardisation of the segmentation protocol. Calculations based on exported RV meshes were all deterministic, and therefore did not introduce any additional variation.

Study outcomes were limited by the population of ToF patients included in this research. The ToF population had a median LVEF of 54%, only slightly deviating from normal values published for healthy individuals. Mean RVEF in the ToF population was 45%, which is within the normal range (18). Therefore, it can be concluded that a large portion of ToF patients had a cardiac function that would be considered normal in the healthy populations. More significant differences might have been found if research had been performed on a group of ToF patients with more advanced stages of functional degradation.

Lastly, no gold standard parameters exist for the quantification of RV morphology and function assessment. Consequently, clinical significance of computed parameters could not be quantified during this investigation. Usability of proposed methods has yet to be proved, requiring additional research.

4.5. Future research

With the ability to automatically quantify RV morphology and function from dynamic 3D RV meshes, research should be extended to gain more insight in RV remodelling processes. Our patient set was not suitable to investigate long-term follow-up and longitudinal change in RV morphology and function. Longitudinal follow-up of ToF patients may allow for the identification of regions with significant remodelling over time. Hereby, new biomarkers could be identified for clinical deterioration or effective RV remodelling in ToF patients. A proof of concept investigation was performed using three ToF patients with two 3DE studies acquired at different time points. These patients showed progressive dilatation over time. All three patients showed decrease of the AP component of dEF, with an average of 6%. Changing patterns in dEF throughout different stages of disease could grant valuable new information. Other longitudinal research on the prognostic value of regional RV deformation analysis confirmed its added value in patients with pulmonary hypertension (41). Longitudinal follow-up of a larger ToF cohort would be needed for definitive identification of remodelling biomarkers. Potentially interesting parameters identified in this research consist of vcrMC of the PBD, APX, and RVOT, and the AP component of dEF with special attention paid to the AFW region. Eventually, these biomarkers could be of great value in the optimisation of pulmonary valve replacement timing, trading off the limited durability of

artificial pulmonary valves and the prevention of irreversible RV dysfunction.

Besides the investigation of RV morphology and function in ToF patients, research on other patient populations could yield valuable insights in the effect of different diseases on RV remodelling. Earlier research investigated patients with PAH (27, 41). Additionally, a study compared small populations of patients with ToF to patients with PAH. Remodelling effects of volume overload were compared to effects of pressure overload of the RV, revealing distinct differences between patient populations (28). With the developed software application, vcrMC, dEF, and rdEF can be automatically calculated from RV triangulated mesh files, paving the way for researching morphological and functional RV remodelling in any patient population.

5. Conclusion

This thesis enhances the understanding of RV remodelling in ToF patients, by quantifying both global and regional RV morphological and functional characteristics using 3DE imaging. A software application was developed to objectively assess morphological and functional RV remodelling, by calculating vcrMC and dEF of the RV. Quantification of vcrMC revealed highly heterogeneous regional curvature changes in ToF patients compared to healthy controls. The PBD, APX, and RVOT regions showed largest decreases in curvature making them highly interesting for further investigation. Directional decomposition of RVEF enabled detailed quantification of RV function in patients with ToF. Deterioration of RV function was mostly assigned to decreased contribution of AP wall motion to RVEF. Deterioration of the AP component of dEF was identified as a distinct remodelling effect of the RV, showing no significant correlation with LVEF. Therefore, dEF in the AP direction was identified as an interesting candidate for assessment of advanced functional RV remodelling in ToF patients. The AFW region was recognised as an important region for functional RV remodelling, showing the same pattern of rdEF as seen in the global RV.

The developed software application enables automatic quantification of RV morphology and RV function from 3DE images. With its development, doors have been opened for researching RV remodelling in any patient population. Future research in ToF patients should focus on longitudinal follow-up, allowing for the identification of regions with significant remodelling over time. Hereby, the proposed parameters can be further evaluated and new biomarkers could be identified for clinical deterioration or effective RV remodelling in ToF patients. Special attention must be paid to regions identified as key contributors to RV remodelling during this research. Eventually, monitoring of these biomarkers could be of great value in the optimisation of pulmonary valve replacement timing in ToF patients.

Supplementary data

S.1 Curvature

Curvature was calculated as a parameter for the quantification of RV morphology. Curvature is defined as the inverse of the radius of the circle osculating the curve of a surface. An osculating circle is a circle touching the curve, such that the circle and curve have an equal tangent. Hereby, the curvature can be represented by the radius of the circle (54). Curvature was calculated for each vertex on the RV mesh. A previously implemented function for curvature calculation in RV-Dynamics (Yue Chen, previous student on this project (33)) was fully checked, documented, and improved during this research. Functions from the OpenGL library were used and programming was performed in Visual Studio 2022 using C++. Several different curvature measures exist and were implemented in the software application, consisting of mean curvature, Gaussian curvature, and principal curvatures. In the final work, mean curvature is reported. Since considerable work was performed in realising, checking and visualising the different curvature measures, the theory and realisation of all curvature variables is presented below.

S.1.1 Voronoi area

In order to calculate the curvature for a vertex, a 3D surface surrounding a vertex must be defined over which the curvature can be determined. Meyer et al. (35) proposed a method for the allocation of surfaces to vertices in a mesh, based on the 1-ring neighbourhood of the vertex. The 1-ring neighbourhood of a vertex consists of the vertices directly neighbouring the vertex. From this 1-ring neighbourhood (x_p, x_q, x_r, x_s, x_t), the Voronoi area of each vertex (x_i) can be determined as a method to evenly allocate surfaces on a mesh to the closest vertex (Figure S1A).

For acute triangles, the Voronoi area can be defined by drawing all perpendicular bisectors of a triangle, coming together in the circumcentre. These lines enclose an area for which vertex x_i is the nearest vertex. For obtuse triangles, two scenarios exist. If the obtuse angle is located at vertex x_i, midpoints of adjacent sides are connected to the midpoint of the opposite side to enclose a surface. If the obtuse angle is not located at vertex x_i, midpoints of adjacent sides are directly connected.

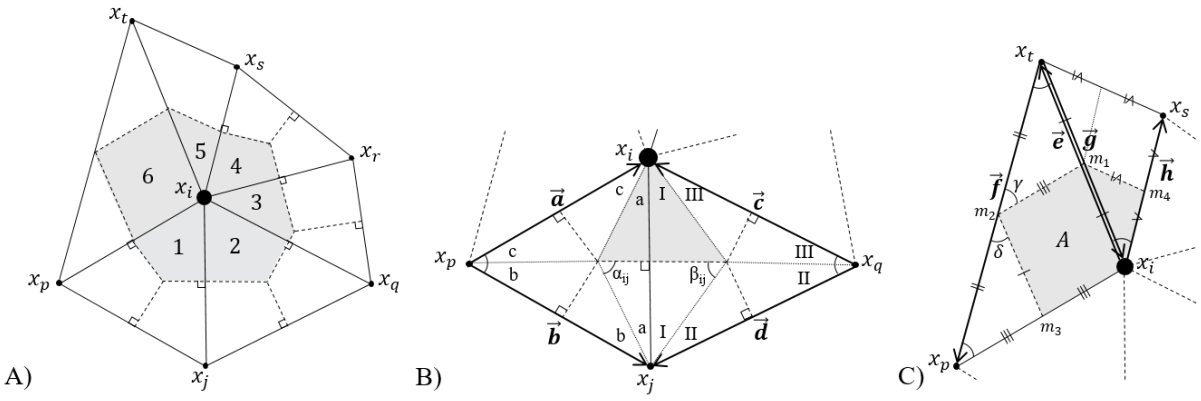

Figure S1: Geometrical calculations of Voronoi area (grey) for vertex x_i, using it's 1-ring neighbourhood. A) Voronoi areas of triangles in 1-ring neighbourhood of vertex x_i, with acute triangles in 1-4, an obtuse triangle with the obtuse angle not at vertex x_i in 5, and an obtuse triangle with the obtuse angle at vertex x_i in 6, B) construction of Voronoi area of an acute triangle, C) construction of Voronoi area of two obtuse triangles.

The Voronoi area of acute triangles can be calculated using the cotangent of angle α_{ij}, angle β_{ij}, and the distance between vertices x_i and x_j (Formula 1):

$$A_{Voronoi} = \frac{1}{8}(\cot\alpha_{ij} + \cot\beta_{ij})\left\|x_i - x_j\right\|^2. \quad (1)$$

Formula 1 is derived from the equation for the calculation of the area of a triangle (A):

$$A = \frac{1}{2} * base * height,$$
$$A = \frac{1}{2} * \left((\cot\alpha_{ij} + \cot\beta_{ij}) * \frac{1}{2}\left\|x_i - x_j\right\|\right) * \left(\frac{1}{2}\left\|x_i - x_j\right\|\right).$$

In any acute triangle, angle α_{ij} happens to be equal to angle x_p. This characteristic can be derived by connecting each vertex of the triangle with the circumcentre (Figure S1B). From triangle $\Delta x_i x_j x_p$ follows that:

$$2a + 2b + 2c = 180°,$$
$$a + b + c = 90°,$$
$$\angle x_p = \alpha_{ij}.$$

Consequently, $\cot\alpha_{ij} = \cot\angle x_p$ which can be calculated from the dot product and cross product of the coordinates of vertices x_i, x_j, and x_p:

$$\cot\angle x_p = \frac{\cos\angle x_p}{\sin\angle x_p},$$
$$\vec{a} = x_i - x_p \text{ and } \vec{b} = x_j - x_p,$$
$$\cos\angle x_p \frac{\vec{a}\cdot\vec{b}}{\|\vec{a}\|\,\|\vec{b}\|} \quad \text{and} \quad \sin\angle x_p = \frac{\vec{a}\times\vec{b}}{\|\vec{a}\|\,\|\vec{b}\|\,\boldsymbol{n}}.$$
$$\text{Therefore, } \cot\angle x_p = \frac{\vec{a}\cdot\vec{b}}{\|\vec{a}\times\vec{b}\|}.$$

Similarly, it can be stated for triangle $\Delta x_i x_q x_j$ that:

$$\angle x_q = \beta_{ij}.$$

Following the same principles as for $\cot\alpha_{ij}$, $\cot\beta_{ij} = \cot\angle x_q$ which can be calculated using the coordinates of vertices x_i, x_j, and x_q:

$$\cot\angle x_q = \frac{\vec{c}\cdot\vec{d}}{\|\vec{c}\times\vec{d}\|},$$
$$\text{where } \vec{c} = x_i - x_q \text{ and } \vec{d} = x_j - x_q.$$

For obtuse triangles, two different formulas were used; one for triangles where the obtuse angle is at x_i and one for triangles where the obtuse angle is not at x_i (Figure S1C). The Voronoi area of an obtuse triangle where the obtuse angle is at x_i, can be calculated using connecting lines between the midpoints of adjacent sides and the midpoint of the opposite side (Formula 2):

$$\frac{|x_t m_1|}{|x_t x_i|} = \frac{|m_2 x_t|}{|x_p x_t|} = \frac{|m_1 m_3|}{|x_i x_p|} = \frac{1}{2},$$
$$\text{therefore, } \angle x_p = \angle\gamma \text{ and } \angle x_t = \angle\delta.$$

Calculating the areas of $\Delta x_t m_1 m_2$ and $\Delta x_t x_i x_p$ gives:

$$A_{\Delta x_t m_1 m_2} = \frac{1}{2} * |x_t m_2| * (\sin \angle x_t * |x_t m_1|),$$
$$A_{\Delta x_t x_i x_p} = \frac{1}{2} * 2|x_t m_2| * (\sin \angle x_t * 2|x_t m_1|).$$
$$\text{Therefore, } A_{\Delta x_t m_1 m_2} = \frac{1}{4} A_{\Delta x_t x_i x_p}.$$

The same calculation can be made for $\Delta m_2 m_3 x_p$ and $\Delta x_t x_i x_p$:

$$A_{\Delta m_2 m_3 x_p} = \frac{1}{4} A_{\Delta x_t x_i x_p}.$$

Therefore, the Voronoi area for an obtuse triangle where the obtuse angle is at x_i, is calculated by:

$$A = A_{\Delta x_t x_i x_p} - A_{\Delta x_t m_1 m_2} - A_{\Delta m_2 m_3 x_p},$$
$$A = \frac{1}{2} A_{\Delta x_t x_i x_p}. \quad (2)$$

The area of $\Delta x_t x_i x_p$ can be calculated from the cross product of the coordinates of vertices x_t, x_i, and x_p:

$$\vec{e} = x_i - x_t \text{ and } \vec{f} = x_p - x_t,$$
$$A_{\Delta x_t x_i x_p} = \frac{1}{2} \left\| \vec{e} \times \vec{f} \right\|.$$

The Voronoi area of an obtuse triangle where the obtuse angle is not at x_i can be calculated using a line connecting the midpoints of the adjacent sides (Formula 3):

$$\frac{|m_4 x_i|}{|x_s x_i|} = \frac{|x_i m_1|}{|x_i x_t|} = \frac{|m_1 m_4|}{|x_t x_s|} = \frac{1}{2}.$$

Calculating the areas of $\Delta m_4 x_i m_1$ and $\Delta x_s x_i x_t$ gives:

$$A_{\Delta m_4 x_i m_1} = \frac{1}{2} * |x_i m_1| * (\sin \angle x_i * |m_4 x_i|),$$
$$A_{\Delta x_s x_i x_t} = \frac{1}{2} * 2|x_i m_1| * (\sin \angle x_i * 2|m_4 x_i|).$$
$$\text{Therefore, } A_{\Delta m_4 x_i m_1} = \frac{1}{4} A_{\Delta x_s x_i x_t}. \quad (3)$$

The area of $\Delta x_s x_i x_t$ can be calculated from the cross product of the coordinates of vertices from x_s, x_i, and x_t:

$$\vec{g} = x_t - x_i \text{ and } \vec{h} = x_s - x_i,$$
$$A_{\Delta x_s x_i x_t} = \frac{1}{2} \left\| \vec{g} \times \vec{h} \right\|.$$

By adding up separately calculated areas for each triangle, the total Voronoi area attributed to vertex x_i can be determined (Formulas 1-3). This area is used as the surface over which curvatures are calculated.

S.1.2 Principal curvature

Meyer at al. (35) described two types of curvature which can be used for the characterization of a surface shape: Gaussian curvature and mean curvature. These curvatures are derivatives of the principal curvatures of a surface.

For each vertex, principal curvatures can be determined by intersecting the surface at multiple angles, using a plane positioned orthogonal to the tangent plane (t) of vertex (x_i). These orthogonal intersections are used as means to visualise two-dimensional (2D) curves of the 3D surface. Principal curvatures are defined as the inverses of radii (r_1 and r_2) of the imaginary circles osculating the 2D curves at angles yielding maximum (k_1) and minimum (k_2) curvature values for each vertex (Figure S2) (34).

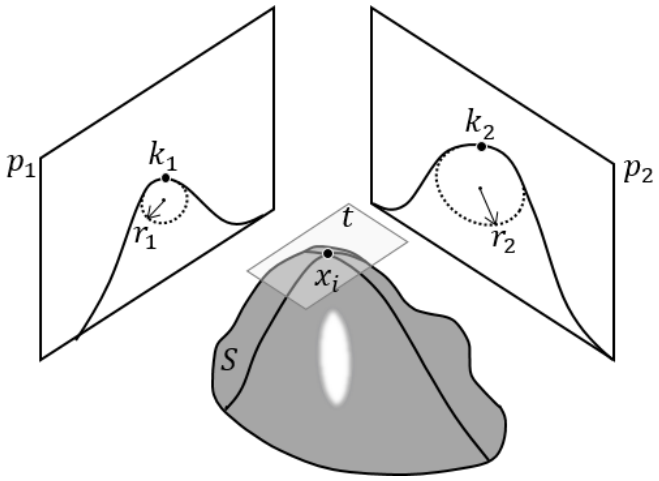

Figure S2: Schematic representation of principal curvature (k_1 and k_2) definitions for a vertex (x_i) on a surface (S), derived from the radii (r_1 and r_2) of two circles osculating the curves projected on two orthogonal planes (p_1 and p_2) intersecting the surface orthogonal to the tangent plane (t).

Principal curvatures k_1 and k_2 of vertex x_i can be computed from the mean curvature (MC) and the Gaussian curvature (GC) of the vertex:

$$k_1(x_i) = MC(x_i) + \sqrt{MC(x_i)^2 - GC(x_i)}, \quad (4)$$

$$k_2(x_i) = MC(x_i) - \sqrt{MC(x_i)^2 - GC(x_i)}. \quad (5)$$

S.1.3 Gaussian curvature

Gaussian curvature (GC) quantifies the presence of curvature in both principal curvature directions of a surface, and whether these curvatures are directed in equal or opposite direction. If both principal curvatures are pointing in the same direction, GC is bigger than 0. GC is 0 if one of the principal curvatures is 0. If the principal curvatures are pointing in opposite directions, GC has a value smaller than 0 (34).

$GC$of vertex x_i can be defined as function of principal curvatures:

$$GC(x_i) = k_1(x_i) * k_2(x_i). \quad (6)$$

A discrete definition uses the sum of angles (θ_i) in radians between vertex x_i and the vertices in its one ring neighbourhood. Consequently, the remaining angle is divided by the Voronoi area ($A_{Voronoi}$), as shown in Formula 7 (35). Angle θ_i can be calculated from the dot product of the coordinates of vertices x_i, x_j, and x_p. An example of the calculation of GC for a single triangle can be seen in Figure S3.

$$GC(x_i) = \frac{2\pi - \sum \theta_i}{A_{Voronoi}}, \tag{7}$$

where $\angle\theta_i = \text{acos}\frac{\overrightarrow{x_i x_j} \cdot \overrightarrow{x_i x_p}}{\|\overrightarrow{x_i x_j}\| \, \|\overrightarrow{x_i x_p}\|}$.

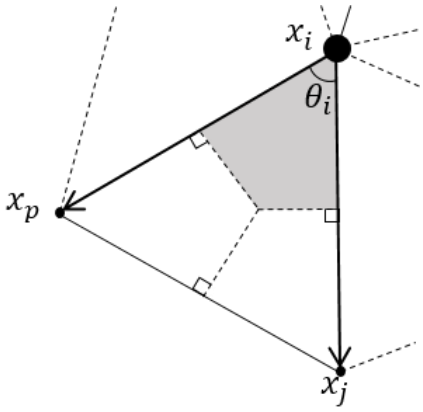

Figure S3: Geometry for the calculation of Gaussian curvature for the triangle formed by vertex x_i and neighbouring vertices x_p and x_j, with the Voronoi area (grey) and angle θ_i.

S.1.4 Mean curvature

Mean curvature (MC) is the average curvature of a surface in 3D space. It can be calculated by intersecting the surface at an infinite amount of angles, using a plane positioned orthogonal to the tangent plane of a vertex. On these orthogonal intersections, imaginary osculating circles can be fitted from which curvature can be calculated as inverse of their radii. Taking the mean of this infinite amount of curvatures yields the MC. A negative MC signifies a concave surface and a positive MC a convex surface (34).

MC of vertex x_i can be derived from the two principal curvatures k_1 and k_2:

$$MC(x_i) = \frac{k_1(x_i) + k_2(x_i)}{2}. \tag{8}$$

A discrete definition of MC can be given as function of angle α_{ij}, angle β_{ij}, and vertices x_i and x_j (Figure S4). This calculation is summed over all vertices in the 1-ring neighbourhood of vertex x_i ($N_1(i)$), and divided by the Voronoi area ($A_{Voronoi}$) (35):

$$MC(x_i) = \frac{1}{2}\left\| \frac{1}{2 * A_{Voronoi}} \sum_{j \in N_1(i)} \left(\cot \alpha_{ij} + \cot \beta_{ij}\right)(x_i - x_j) \right\|. \tag{9}$$

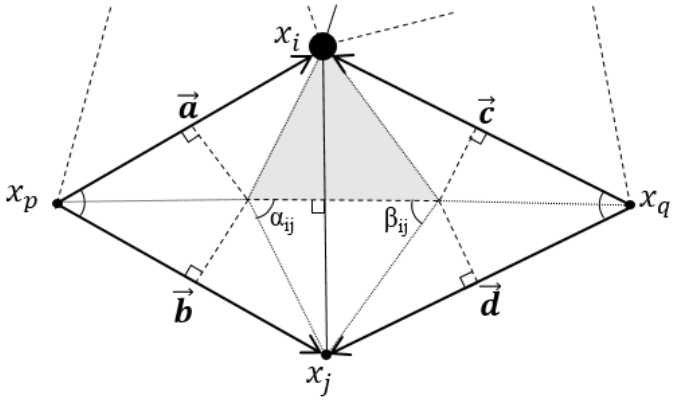

Figure S4: Geometry for the calculation of mean curvature for vertex x_i and its neighbouring vertex x_j, with the Voronoi area (grey).

Voronoi area is calculated according to the method described in S.1.1 Voronoi area. Cotangents of angle α_{ij} and angle β_{ij} were computed from the coordinates of vertex x_i and vertices in the 1-ring neighbourhood using their dot product and cross product according to the approach for Formula 1:

$$\cot \angle x_p = \cot \alpha_{ij} = \frac{\vec{a} \cdot \vec{b}}{\|\vec{a} \times \vec{b}\|} \quad \text{and} \quad \cot \angle x_q = \cot \beta_{ij} = \frac{\vec{c} \cdot \vec{d}}{\|\vec{c} \times \vec{d}\|}.$$

Vector $\overrightarrow{x_j x_i}$ is weighed by the length of the perimeter of the Voronoi area of vertex x_i that is allocated to neighbouring vertex x_j, by multiplying with $\cot \alpha_{ij}$ and $\cot \beta_{ij}$. Hereby, relative contribution of the vector to the calculated MC is determined. Summation of all weighted vectors belonging to the vertices in the 1-ring neighbourhood, and dividing by the Voronoi area leads to a vector representing MC of the surface belonging to vertex x_i. The magnitude of MC is equal to the magnitude of the summation vector. The direction of MC is determined using normal vector $\vec{\boldsymbol{n}}$ of the surface. Normal vector $\vec{\boldsymbol{n}}$ is always pointed outward of the beutel, due to the positive orientation of the mesh. MC is negative if pointing in the same direction as $\vec{\boldsymbol{n}}$, and positive if pointing in the opposite direction (Figure S5).

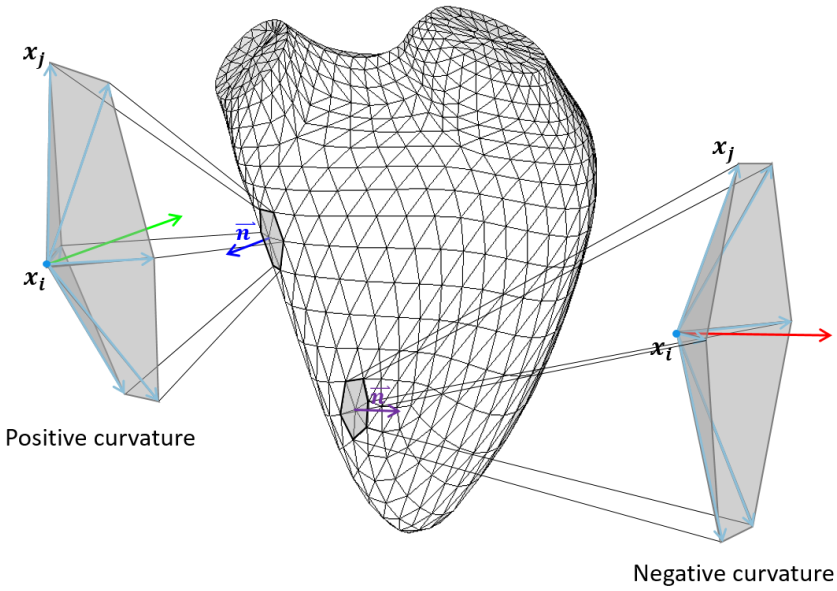

Figure S5: Discrete calculation of mean curvature for vertex x_i. A summation vector is generated by taking the weighted average of vectors between x_i and all vertices in its 1-ring neighbourhood (cyan). The summation vector is divided by the Voronoi area. A summation vector (green) in the direction opposite to the normal vector (blue) results in positive curvature. A summation vector (red) in the same direction as the normal vector (purple) results in negative curvature.

MC was determined to be more suitable and intuitive as measure for curvature of dynamic RV surface meshes than GC. MC was therefore computed and analysed for each patient in ED and ES frames in this research.

S.1.5 Volume correction

ToF patients are notorious for developing RV dilatation over time, caused by RV volume overload (15). As curvature is the inverted radius of the circle osculating the surface curve, measured curvatures will be smaller in larger ventricles. As a result, curvature values of dilated RV will be smaller than curvature of healthy RV. To prevent only quantifying dilatation effects instead of remodelling in ToF patients, volume correction was performed on all curvature measurements. An adaptation of the method proposed by Addetia et al. (27) was applied. MC

values were divided by a normalisation term (k_{reg}), which was calculated as the curvature of a sphere $\left(\frac{1}{r}\right)$ with the same volume as the RV of the subject (V_{sphere}):

$$V_{sphere} = \frac{4}{3}\pi r^3,$$
$$k_{reg} = \frac{1}{r} = \sqrt[3]{\frac{4\pi}{3V_{sphere}}}. \quad (10)$$

The normalisation term was based on RV EDV for ED MC calculations and on RV ESV for ES MC calculations. Volume correction resulted in a volume corrected mean curvature value ($vcMC$) (Formula 11). This value is a ratio between curvatures, and was presented as a percentage during this research.

$$vcMC(x_i) = \frac{MC(x_i)}{k_{reg}}. \quad (11)$$

S.1.6 Region definition

Eleven different regions were defined for regional MC calculation, based on literature and expert opinion (28, 37, 38). Vertices were each assigned to one of these regions, after which the regional average was determined. Morphological features of interest were taken into account by dividing the regions such that these characteristics could be optimally quantified (Figure 3).

Right ventricular inflow tract (RVIT): defined for the quantification of shape of the tricuspid annulus region. Six rows of vertices surrounding the tricuspid valve were allocated to the RVIT region, forming a cylindrical inflow region.

Right ventricular outflow tract (RVOT): defined for the quantification of shape of the pulmonary annulus region. Three rows of vertices encircling the pulmonary valve make up a cylindrical outflow region.

Infundibulum: region in between the RVIT and RVOT forming a saddle shape. This region was not assessed in this research and was not mentioned in analyses due to its heterogeneous saddle shape. Saddle shapes cannot be quantified meaningfully using MC, as positive and negative curvatures cancel each other out.

Anterior free wall (AFW): defined for the quantification of shape of the free wall area directed towards the RVOT. This region forms a triangular area from the RV base to the apex, and has approximately the same basal width as the RVOT.

Inferior free wall (IFW): defined for the quantification of shape of the free wall area directing away from the RVIT. This region forms a triangular area from the RV base to the apex, and has approximately half the basal width of the RVIT.

Lateral free wall (LFW): region that is positioned in between the AFW and IFW regions.

Septum: defined for the assessment of the shape of the interventricular septum. This region forms a triangular area, starting directly below the RVIT, infundibulum, and RVOT, and reaches down to the apex. The septum proved to be susceptible for mixing of very different curvatures as a result of variation in boundary regions, coming together in the septum region. Therefore, the septum was not assessed during curvature analyses of this research. Instead, a subsection of the septum was defined for curvature quantification of the septum, named the septal body.

Septal body (SPB): defined for the calculation of septal curvature from a smaller selection of vertices in the septum region. Hereby, most explicit curvature of the septum could be quantified in a consistent manner, decreasing susceptibility for patient-to-patient variation in boundary regions coming together in the septum region. This region was analysed instead of the complete septum.

Anterior boundary (ABD): defined for the quantification of shape of the boundary between the AFW and septum region. The region forms a strip with a width of three vertices between the AFW and septum, reaching from the RVOT down to the apex.

Posterior boundary (PBD): defined for the quantification of shape of the boundary between the IFW and septum region. The region forms a strip with a width of three vertices between the IFW and septum, reaching from the RVIT down to the apex.

Apex (APX): defined for the quantification of apical curvature. This region is formed by ten vertices on the bottom of the RV, surrounding the lowest point of the RV mesh.

S.1.7 Visualisation

A visualisation tool was previously developed (Gerard van Burken and Yue Chen) for qualitative morphological assessment of regional MC of individual RV beutels. This tool uses functions from the OpenGL library, visualised in a graphical user interface based on Dear ImGui, and was written in Microsoft Visual Studio 2022 using C++. Adaptations and improvements were made during this research for the visualisation of volume corrected MC, and to improve usability. Curvatures were displayed per vertex, using a heat map projected on the RV mesh. Novel colour coding was implemented. Vertices with the most negative MC were displayed as blue, transitioning to cyan for values closer to zero. Vertices with maximal positive MC were visualised as red, transitioning to yellow for values closer to zero. Outliers were not taken into account in determining minimum and maximum values for the colour distribution. The highest and lowest 5% of MC values of a subject were classified as outliers, and displayed as red or blue respectively. Colours (c) were interpolated using an arctangent function:

$$k_{norm} = \begin{cases} \frac{|vcMC(x_i)|}{|vcMC_{min}|} & if\ k_{H_V} < 0 \\ \frac{vcMC(x_i)}{vcMC_{max}} & if\ k_{H_V} > 0 \end{cases},$$
$$f = \frac{2*\mathrm{atan}(3k_{norm})}{\pi},$$
$$c = \begin{cases} (1-f) * green + blue & if\ vcMC < 0 \\ (1-f) * green + red & if\ vcMC > 0 \end{cases}. \quad (12)$$

These calculations result in a colour distribution shown in the colour bar in Figure S6.

Figure S6: Colour bar used for displaying volume corrected mean curvature by overlapping a RV mesh with a heat map. Max=maximum volume corrected mean curvature value of the RV; Min=minimum volume corrected mean curvature value of the RV.

S.1.8 Validation of curvature calculation

Validation of curvature calculations was performed by calculating MC and $vcMC$ values of a known shape. An icosahedron shape was used, consisting of 12 vertices making up 20 triangles. Three different configurations of the icosahedron were used, to test robustness of the

calculations. Test shape 1 was a basic icosahedron with a radius of 1 cm (Figure S7A). Test shape 2 was scaled by a factor 2, leading to an icosahedron with a radius of 2 cm (Figure S7B). The third test shape was an icosahedron with a radius of 1 cm that was mirrored in the x-axis, leading to an inverted shape with negative orientation (Figure S7C). Calculations led to the values presented in Table S1. These values were exactly as expected for MC and $vcMC$ calculations of these shapes.

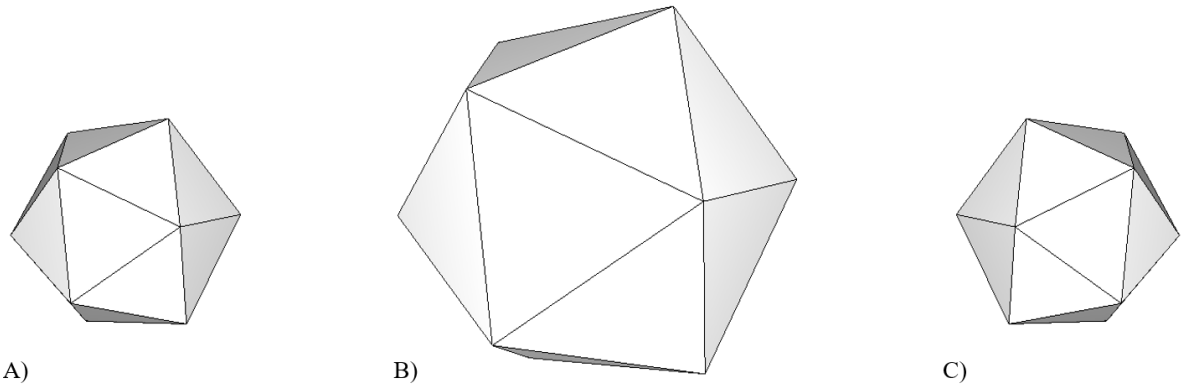

Figure S7: Icosahedron shapes used for the validation of mean curvature and volume corrected mean curvature calculations. A) Icosahedron with a radius of 1 cm, B) icosahedron with a radius of 2 cm, C) icosahedron with a radius of 1 cm, mirrored in the x-axis.

Table S1: Validation of mean curvature and volume corrected mean curvature calculation using three test shapes.

Test shape	Volume (mL)	Mean curvature (cm^{-1})	Volume corrected mean curvature (-)
1	2.5	1	0.85
2	20.3	0.5	0.85
3	2.5	-1	-0.85

Test shape 1: icosahedron with a radius of 1 cm; test shape 2: icosahedron with a radius of 2 cm; test shape 3: icosahedron with a radius of 1 cm, mirrored in the x-axis.

S.2 Decomposed ejection fraction

Detailed quantification of RV function was achieved through the decomposition of RV contraction into three anatomical directions. RV wall motion was decomposed in anteroposterior (AP), radial (RD), and longitudinal (LT) direction, in line with literature findings (39, 40). A novel function was implemented in RV-Dynamics for the calculation of decomposed RV contraction. Functions from the OpenGL library were used and programming was performed in Visual Studio 2022 using C++.

S.2.1 Axis definition

In order for the decomposition to be performed in a consistent manner, the coordinate system had to be standardised for each beutel. Three reference vertices were used for the definition of an anatomical coordinate system. These vertices consisted of the apex, centre point of the tricuspid valve, and centre point of the pulmonary valve. TomTec 4D RV-Function outputs structured meshes with a fixed topology and anatomical vertex correspondence for each beutel. As a result, vertices belonging to specific anatomical locations can easily be extracted from the mesh files. First, an imaginary line was drawn between the centre points of both valves, named the intervalvular line. The direction of the LT-axis was defined from the apex to the midpoint of the intervalvular line. Subsequently, the direction of the RD-axis was determined perpendicular to the LT-axis and the intervalvular line, using the cross product of these two vectors (Figure S8A). Lastly, the direction of the AP-axis was defined perpendicular to the LT- and RD-axis, using the cross product of these two axes. The anatomical coordinate system was

defined to have its origin in the RV centre of mass in the systolic frame, with unit vectors in the AP, RD and LT axis directions. Anatomical alignment was performed by rotation around this origin to align the x-axis with the AP-axis, the y-axis with RD-axis, and the z-axis with LT-axis (Figure S8B). Hereby, each beutel was oriented in a standardised anatomical coordinate system. Coordinate system definition was based on the approach described by Tokodi et al. (40), and adapted in discussion with clinical and technical partners involved in this project.

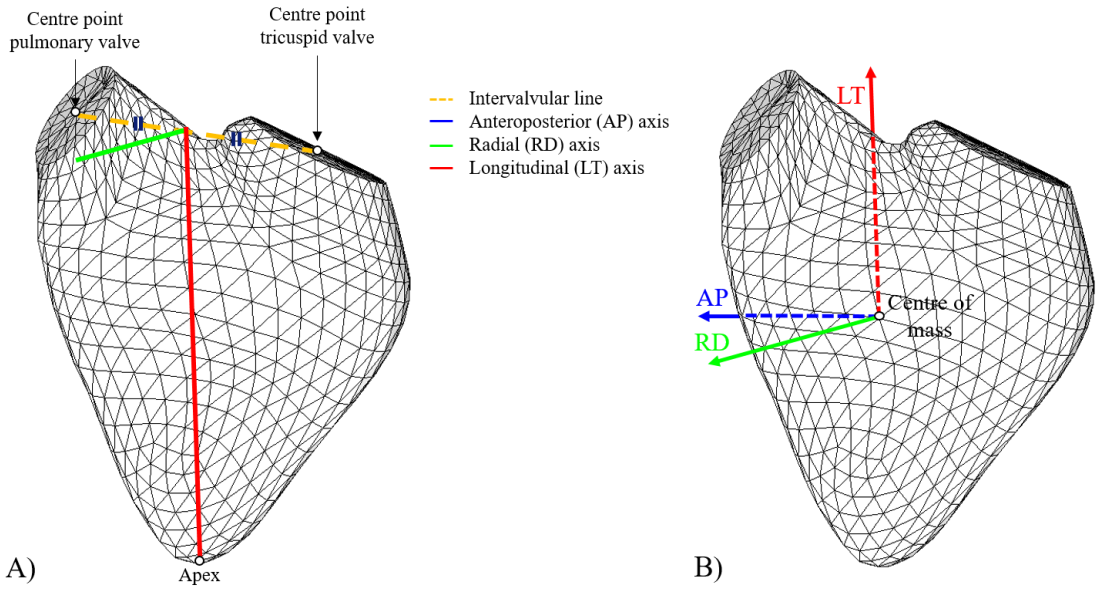

Figure S8: Axis definition and beutel orientation. A) Direction of the longitudinal axis (red) from the apex to the midpoint of the intervalvular line (orange) and the direction of the radial axis (green) perpendicular to the longitudinal axis and intervalvular line, B) anteroposterior (blue), radial (green), and longitudinal (red) axes after translation, locating the origin on the centre of mass at end-systole. AP: anteroposterior; RD: radial; LT: longitudinal.

S.2.2 Mesh decomposition

A set of meshes was available from TomTec 4D-RV Function for each patient, representing t different time frames during the cardiac cycle. The amount of available frames differs per patient, depending on heart rate and frame rate. Each mesh consists of a list of k vertices ($v_{1:k}$), for which its position is described in terms of an x-, y-, and z-coordinate. After standardisation of the coordinate system, the x-axis corresponds to the AP direction, the y-axis to the RD direction, and the z-axis to LT direction. For the computation of directional wall motion, only one of the coordinates is allowed to vary whilst the other two are kept constant on their ED value. Hereby, only movement in the direction of the deviating coordinate can be studied. For AP wall motion, the x-coordinate changes over time ($x_1, \dots, x_t$) while the y- and z-coordinate are kept constant (y_{ED} and z_{ED}). For RD wall motion, the y-coordinate changes over time ($y_1, \dots, y_t$) while the x- and z-coordinate are kept constant (x_{ED} and z_{ED}). Lastly, for LT wall motion, the z-coordinate changes over time ($z_1, \dots, z_t$) while the x- and y-coordinate are kept constant at the ED value (x_{ED} and y_{ED}). This results in three sets of decomposed meshes, each representing motion in one of three anatomical directions.

From these sets of decomposed meshes, EF can be calculated by looking at the ED and ES decomposed mesh volumes ($dEDV$ and $dESV$). Decomposed mesh volumes were calculated using the signed tetrahedron method (36). Subsequently, EF was calculated using Formula 12. These calculations resulted in values for decomposed EF (dEF) in AP direction, dEF in RD direction, and dEF in LT direction.

$$dEF = \frac{dEDV - dESV}{dEDV} \quad (12)$$

S.2.3 Relative decomposed EF

For relative decomposed EF ($rdEF$) calculation, dEF in AP direction, dEF in RD direction, and dEF in LT direction were divided by the sum of all three dEF components. Hereby, a value could be established which represents the fraction of EF brought about by a single motion direction. These calculations resulted in $rdEF$ values in longitudinal ($rdEF_{LT}$), radial ($rdEF_{RD}$), and anteroposterior ($rdEF_{AP}$) directions:

$$rdEF_{LT} = \frac{dEF_{LT}}{dEF_{LT}+dEF_{RD}+dEF_{AP}},$$
$$rdEF_{RD} = \frac{dEF_{RD}}{dEF_{LT}+dEF_{RD}+dEF_{AP}},$$
$$rdEF_{AP} = \frac{dEF_{AP}}{dEF_{LT}+dEF_{RD}+dEF_{AP}}. \quad (13)$$

S.2.4 Region definition

For the assessment of regional contributions to EF, RV meshes were divided into four regions. Hereby, regional RV function could be quantified. Regions differed from the ones used for regional MC calculation, enlarging regional volumes to decrease sensitivity to local volumetric changes. For the calculation of dEF and $rdEF$, partial volumes were computed in ED and ES frames of decomposed meshes, spanned between the regional surface and ES centre of mass. Regions were defined based on literature and expert opinion (Figure 6) (28, 41).

Anterior free wall (AFW): defined for the quantification of RV function of the free wall area directed towards the pulmonary valve. This region forms a triangular area from the pulmonary valve to the apex.

Inferior free wall (IFW): defined for the quantification of RV function of the free wall area directing blood from the tricuspid valve. This region forms a triangular area from the tricuspid valve to the apex.

Lateral free wall (LFW): region that is located in between the AFW and IFW regions.

Septum: this region forms a triangular area, starting from the tricuspid valve and pulmonary valve, reaching down to the apex. The septum region was not assessed and included in analyses in this research. As a result of the volume calculation method applied, EF turned out negative for specific patients leading to meaningless measurements.

S.1.8 Validation of decomposed ejection fraction calculation

Validation of dEF calculations was performed using a similar method as for the validation of MC calculations. Seven different configurations of the icosahedron were used as ED shapes, to test robustness of the calculations. A basic icosahedron with radius of 1 cm was used for each calculation as ES shape. Test shape 1 was scaled by a factor 2 in the AP direction (Figure S9A), test shape 2 was scaled by a factor of 2 in the RD direction (Figure S9B), and test shape 3 was scaled by a factor of 2 in the LT direction (Figure S9C). The fourth test shape was scaled with a factor 2 in the AP, RD, and LT direction (Figure S9D). Test shape 5 was similar to test shape 1, but translated according to translation vector $T\langle 10, 10, 10\rangle$. The sixth test shape was rotated along the x-axis towards a y-axis of $[0, 0.5, 0.866]$ and a z-axis of $[-0.866, 0.5, 0]$. Lastly, test shape 7 was similar to test shape 1 but mirrored in the x-axis. Calculations led to the values presented in Table S2. These values were exactly as expected for dEF calculations for these shapes.

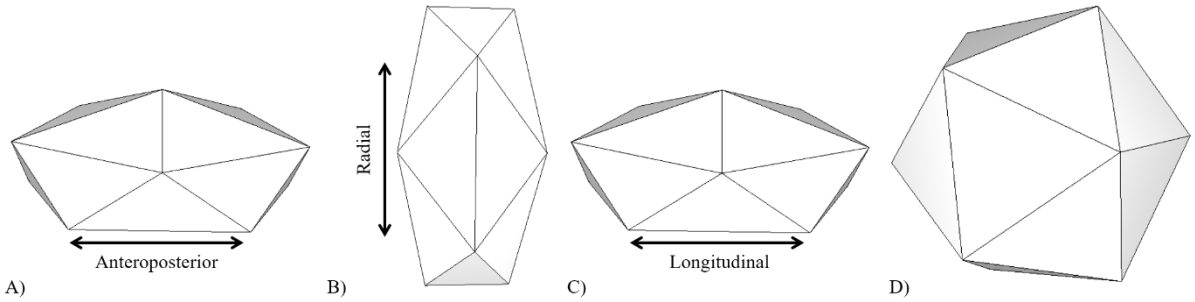

Figure S9: Icosahedron shapes used for the validation of decomposed ejection fraction calculations. A) Icosahedron with a radius of 1 cm, scaled with factor 2 in the AP direction, B) icosahedron with a radius of 1 cm, scaled with factor 2 in the RD direction, C) icosahedron with a radius of 1 cm, scaled with factor 2 in the LT direction, D) icosahedron with a radius 1 cm, scaled with factor 2 in the AP, RD, and LT direction. AP: anteroposterior; RD: radial; LT: longitudinal.

Table S2: Validation of decomposed ejection fraction calculation using seven test shapes.

		Decomposed ejection fraction		
Test shape	Global	Anteroposterior	Radial	Longitudinal
1	50	50	0	0
2	50	0	50	0
3	50	0	0	50
4	87.5	50	50	50
5	50	50	0	0
6	50	50	0	0
7	50	50	0	0

Values are presented as percentages. 1: icosahedron with a radius of 1 cm, scaled with factor 2 in the AP direction 2: icosahedron with a radius of 1 cm, scaled with factor 2 in the RD direction; 3: icosahedron with a radius of 1 cm, scaled with factor 2 in the LT direction; 4: icosahedron with a radius of 1 cm, scaled with factor 2 in the AP, RD, and LT direction; 5: test shape 1, translated in the AP, RD, and LT direction; 6: test shape 1, rotated along x-axis; 7: test shape 1, mirrored in the x-axis. AP: anteroposterior; RD: radial; LT: longitudinal.

S.3 Supplementary results

Table S3: End-diastolic and end-systolic regional mean curvature in ToF and healthy controls.

	End-diastolic			End-systolic		
Region	ToF (n=50)	Controls (n=50)	p-value	ToF (n=50)	Controls (n=50)	p-value
Global	30 [27 - 32]	37 [34 - 40]	<0.001	37 [32 - 40]	54 [48 - 58]	<0.001
Free wall	24 [21 - 26]	28 [25 - 31]	<0.001	26 [24 - 29]	37 [31 - 42]	<0.001
AFW	16 [13 - 20]	23 [17 - 28]	<0.001	16 [13 - 21]	23 [18 - 33]	<0.001
LFW	22 [20 - 25]	27 [24 - 29]	<0.001	26 [22 - 30]	37 [31 - 47]	<0.001
IFW	31 [27 - 35]	34 [31 - 37]	0.002	36 [31 - 39]	41 [36 - 49]	<0.001
ABD	149 [132 - 175]	160 [146 - 189]	0.043	187 [166 - 223]	221 [182 - 268]	0.001
PBD	73 [65 - 87]	98 [83 - 111]	<0.001	99 [83 - 122]	155 [136 - 204]	<0.001
APX	130 [120 - 160]	181 [163 - 205]	<0.001	139 [129 - 192]	247 [197 - 282]	<0.001
SPB	-14 [-20 - -11]	-21 [-27 - -17]	<0.001	-16 [-21 - -13]	-29 [-34 - -22]	<0.001
RVIT	29 [23 - 30]	37 [31 - 40]	<0.001	35 [28 - 40]	51 [41 - 59]	<0.001
RVOT	31 [27 - 34]	42 [38 - 49]	<0.001	38 [30 - 42]	57 [50 - 63]	<0.001

Values are presented as curvature values [m^{-1}], median [interquartile range]. ToF: Tetralogy of Fallot; AFW: anterior free wall; LFW: lateral free wall; IFW: inferior free wall; ABD: anterior boundary; PBD: posterior boundary: APX: apex; SPB: septal body; RVIT: right ventricular inflow tract; RVOT: right ventricular outflow tract.

References

1. Abqari S, Gupta A, Shahab T, Rabbani MU, Ali SM, Firdaus U. Profile and risk factors for congenital heart defects: A study in a tertiary care hospital. Ann Pediatr Cardiol. 2016;9(3):216-21.
2. Becker AE, Connor M, Anderson RH. Tetralogy of Fallot: a morphometric and geometric study. Am J Cardiol. 1975;35(3):402-12.
3. Van Praagh R, Van Praagh S, Nebesar RA, Muster AJ, Sinha SN, Paul MH. Tetralogy of Fallot: underdevelopment of the pulmonary infundibulum and its sequelae. Am J Cardiol. 1970;26(1):25-33.
4. Wilson R, Ross O, Griksaitis MJ. Tetralogy of Fallot. BJA Educ. 2019;19(11):362-9.
5. Bailliard F, Anderson RH. Tetralogy of Fallot. Orphanet J Rare Dis. 2009;4:2.
6. Mainwaring RD, Hanley FL. Tetralogy of Fallot Repair: How I Teach It. Ann Thorac Surg. 2016;102(6):1776-81.
7. Sommer RJ, Hijazi ZM, Rhodes JF. Pathophysiology of congenital heart disease in the adult: part III: Complex congenital heart disease. Circulation. 2008;117(10):1340-50.
8. Tale E, Nikakis J, Malkov D, Arora U, Jose J, Cohen T. A 58-Year Follow-up of Complete Surgical Correction of Tetralogy of Fallot: A Marvel of Modern Medicine. EP Lab Digest 2022.
9. Gatzoulis MA, Balaji S, Webber SA, Siu SC, Hokanson JS, Poile C, et al. Risk factors for arrhythmia and sudden cardiac death late after repair of tetralogy of Fallot: a multicentre study. Lancet. 2000;356(9234):975-81.
10. Ghai A, Silversides C, Harris L, Webb GD, Siu SC, Therrien J. Left ventricular dysfunction is a risk factor for sudden cardiac death in adults late after repair of tetralogy of Fallot. J Am Coll Cardiol. 2002;40(9):1675-80.
11. Therrien J, Siu SC, McLaughlin PR, Liu PP, Williams WG, Webb GD. Pulmonary valve replacement in adults late after repair of tetralogy of fallot: are we operating too late? J Am Coll Cardiol. 2000;36(5):1670-5.
12. Stark J, Bull C, Stajevic M, Jothi M, Elliott M, de Leval M. Fate of subpulmonary homograft conduits: determinants of late homograft failure. J Thorac Cardiovasc Surg. 1998;115(3):506-14; discussion 14-6.
13. van der Ven JPG, van den Bosch E, Bogers A, Helbing WA. Current outcomes and treatment of tetralogy of Fallot. F1000Res. 2019;8.
14. Baumgartner H, De Backer J, Babu-Narayan SV, Budts W, Chessa M, Diller GP, et al. 2020 ESC Guidelines for the management of adult congenital heart disease. Eur Heart J. 2021;42(6):563-645.
15. Ammash NM, Dearani JA, Burkhart HM, Connolly HM. Pulmonary regurgitation after tetralogy of Fallot repair: clinical features, sequelae, and timing of pulmonary valve replacement. Congenit Heart Dis. 2007;2(6):386-403.
16. Larios G, Friedberg MK. Imaging in repaired tetralogy of Fallot with a focus on recent advances in echocardiography. Curr Opin Cardiol. 2017;32(5):490-502.
17. Li W, West C, McGhie J, van den Bosch AE, Babu-Narayan SV, Meijboom F, et al. Consensus recommendations for echocardiography in adults with congenital heart defects from the International Society of Adult Congenital Heart Disease (ISACHD). Int J Cardiol. 2018;272:77-83.
18. Lang RM, Badano LP, Mor-Avi V, Afilalo J, Armstrong A, Ernande L, et al. Recommendations for cardiac chamber quantification by echocardiography in adults: an update from the American Society of Echocardiography and the European Association of Cardiovascular Imaging. J Am Soc Echocardiogr. 2015;28(1):1-39 e14.
19. Kutty S, Zhou J, Gauvreau K, Trincado C, Powell AJ, Geva T. Regional dysfunction of the right ventricular outflow tract reduces the accuracy of Doppler tissue imaging

assessment of global right ventricular systolic function in patients with repaired tetralogy of Fallot. J Am Soc Echocardiogr. 2011;24(6):637-43.
20. Apostolopoulou SC, Manginas A, Kelekis NL, Noutsias M. Cardiovascular imaging approach in pre and postoperative tetralogy of Fallot. BMC Cardiovasc Disord. 2019;19(1):7.
21. Ho SY, Nihoyannopoulos P. Anatomy, echocardiography, and normal right ventricular dimensions. Heart. 2006;92 Suppl 1(Suppl 1):i2-13.
22. Grewal J, Majdalany D, Syed I, Pellikka P, Warnes CA. Three-dimensional echocardiographic assessment of right ventricular volume and function in adult patients with congenital heart disease: comparison with magnetic resonance imaging. J Am Soc Echocardiogr. 2010;23(2):127-33.
23. Ferraro AM, Harrild DM, Powell AJ, Levy PT, Marx GR. Evolving Role of Three-Dimensional Echocardiography for Right Ventricular Volume Analysis in Pediatric Heart Disease: Literature Review and Clinical Applications. J Am Soc Echocardiogr. 2024;37(6):634-40.
24. Medvedofsky D, Addetia K, Patel AR, Sedlmeier A, Baumann R, Mor-Avi V, et al. Novel Approach to Three-Dimensional Echocardiographic Quantification of Right Ventricular Volumes and Function from Focused Views. J Am Soc Echocardiogr. 2015;28(10):1222-31.
25. Muraru D, Spadotto V, Cecchetto A, Romeo G, Aruta P, Ermacora D, et al. New speckle-tracking algorithm for right ventricular volume analysis from three-dimensional echocardiographic data sets: validation with cardiac magnetic resonance and comparison with the previous analysis tool. Eur Heart J Cardiovasc Imaging. 2016;17(11):1279-89.
26. Rudski LG, Lai WW, Afilalo J, Hua L, Handschumacher MD, Chandrasekaran K, et al. Guidelines for the echocardiographic assessment of the right heart in adults: a report from the American Society of Echocardiography endorsed by the European Association of Echocardiography, a registered branch of the European Society of Cardiology, and the Canadian Society of Echocardiography. J Am Soc Echocardiogr. 2010;23(7):685-713; quiz 86-8.
27. Addetia K, Maffessanti F, Yamat M, Weinert L, Narang A, Freed BH, et al. Three-dimensional echocardiography-based analysis of right ventricular shape in pulmonary arterial hypertension. Eur Heart J Cardiovasc Imaging. 2016;17(5):564-75.
28. Bidviene J, Muraru D, Maffessanti F, Ereminiene E, Kovács A, Lakatos B, et al. Regional shape, global function and mechanics in right ventricular volume and pressure overload conditions: a three-dimensional echocardiography study. Int J Cardiovasc Imaging. 2021;37(4):1289-99.
29. Moceri P, Duchateau N, Gillon S, Jaunay L, Baudouy D, Squara F, et al. Three-dimensional right ventricular shape and strain in congenital heart disease patients with right ventricular chronic volume loading. Eur Heart J Cardiovasc Imaging. 2021;22(10):1174-81.
30. Bidviene J, Muraru D, Kovacs A, Lakatos B, Ereminiene E, Liptai C, et al. Global and regional right ventricular mechanics in repaired tetralogy of Fallot with chronic severe pulmonary regurgitation: a three-dimensional echocardiography study. Cardiovasc Ultrasound. 2021;19(1):28.
31. Surkova E, Kovács A, Lakatos BK, Tokodi M, Fábián A, West C, et al. Contraction patterns of the systemic right ventricle: a three-dimensional echocardiography study. Eur Heart J Cardiovasc Imaging. 2022;23(12):1654-62.
32. Lakatos BK, Nabeshima Y, Tokodi M, Nagata Y, Tősér Z, Otani K, et al. Importance of Nonlongitudinal Motion Components in Right Ventricular Function: Three-Dimensional Echocardiographic Study in Healthy Volunteers. Journal of the American Society of Echocardiography. 2020;33(8):995-1005.e1.

33. Zwaan RR, Chen Y, Bowen DJ, van Burken G, Bosch JG, van den Bosch AE, editors. Exploring Three-Dimensional Right Ventricular Shape and Deformation in Tetralogy of Fallot patients [abstract]. EuroACHD; 2024; London, United Kingdom.
34. Vaillant R. Curvature of a triangle mesh, definition and computation. 2013 [updated 05-2013. Available from: https://rodolphe-vaillant.fr/entry/33/curvature-of-a-triangle-mesh-definition-and-computation.
35. Meyer M, Desbrun M, Schröder P, Barr AH. Discrete Differential-Geometry Operators for Triangulated 2-Manifolds. Visualization and Mathematics III. 2003:35-57.
36. Cha Z, Tsuhan C, editors. Efficient feature extraction for 2D/3D objects in mesh representation. International Conference on Image Processing; 2001 7-10 Oct. 2001; Thessaloniki, Greece.
37. Addetia K, Maffessanti F, Muraru D, Singh A, Surkova E, Mor-Avi V, et al. Morphologic Analysis of the Normal Right Ventricle Using Three-Dimensional Echocardiography-Derived Curvature Indices. J Am Soc Echocardiogr. 2018;31(5):614-23.
38. Haddad F, Hunt SA, Rosenthal DN, Murphy DJ. Right ventricular function in cardiovascular disease, part I: Anatomy, physiology, aging, and functional assessment of the right ventricle. Circulation. 2008;117(11):1436-48.
39. Lakatos B, Tősér Z, Tokodi M, Doronina A, Kosztin A, Muraru D, et al. Quantification of the relative contribution of the different right ventricular wall motion components to right ventricular ejection fraction: the ReVISION method. Cardiovasc Ultrasound. 2017;15(1):8.
40. Tokodi M, Staub L, Budai Á, Lakatos BK, Csákvári M, Suhai FI, et al. Partitioning the Right Ventricle Into 15 Segments and Decomposing Its Motion Using 3D Echocardiography-Based Models: The Updated ReVISION Method. Front Cardiovasc Med. 2021;8:622118.
41. Moceri P, Duchateau N, Baudouy D, Schouver ED, Leroy S, Squara F, et al. Three-dimensional right-ventricular regional deformation and survival in pulmonary hypertension. Eur Heart J Cardiovasc Imaging. 2018;19(4):450-8.
42. Sheehan FH, Ge S, Vick GW, 3rd, Urnes K, Kerwin WS, Bolson EL, et al. Three-dimensional shape analysis of right ventricular remodeling in repaired tetralogy of Fallot. Am J Cardiol. 2008;101(1):107-13.
43. Ouyang R, Leng S, Sun A, Wang Q, Hu L, Zhao X, et al. Detection of persistent systolic and diastolic abnormalities in asymptomatic pediatric repaired tetralogy of Fallot patients with preserved ejection fraction: a CMR feature tracking study. Eur Radiol. 2021;31(8):6156-68.
44. Zhong L, Gobeawan L, Su Y, Tan JL, Ghista D, Chua T, et al. Right ventricular regional wall curvedness and area strain in patients with repaired tetralogy of Fallot. Am J Physiol Heart Circ Physiol. 2012;302(6):H1306-16.
45. Mauger CA, Govil S, Chabiniok R, Gilbert K, Hegde S, Hussain T, et al. Right-left ventricular shape variations in tetralogy of Fallot: associations with pulmonary regurgitation. Journal of Cardiovascular Magnetic Resonance. 2021;23(1):105.
46. Sanchez-Quintana D, Anderson RH, Ho SY. Ventricular myoarchitecture in tetralogy of Fallot. Heart. 1996;76(3):280-6.
47. Jurow K, Gauvreau K, Maschietto N, Prakash A. Growth of the right ventricular outflow tract in repaired tetralogy of Fallot: A longitudinal CMR study. Journal of Cardiovascular Magnetic Resonance. 2024;26(1):100002.
48. Ryan T, Petrovic O, Dillon JC, Feigenbaum H, Conley MJ, Armstrong WF. An echocardiographic index for separation of right ventricular volume and pressure overload. J Am Coll Cardiol. 1985;5(4):918-27.
49. Kingma I, Tyberg JV, Smith ER. Effects of diastolic transseptal pressure gradient on ventricular septal position and motion. Circulation. 1983;68(6):1304-14.

50. Wald RM, Haber I, Wald R, Valente AM, Powell AJ, Geva T. Effects of regional dysfunction and late gadolinium enhancement on global right ventricular function and exercise capacity in patients with repaired tetralogy of Fallot. Circulation. 2009;119(10):1370-7.
51. Luo S, Li J, Yang D, Zhou Y, An Q, Chen Y. Right ventricular outflow tract systolic function correlates with exercise capacity in patients with severe right ventricle dilatation after repair of tetralogy of Fallot. Interact Cardiovasc Thorac Surg. 2017;24(5):755-61.
52. Bitterman Y, Hui W, Fan CS, Kiss A, Mertens L, Wald RM, et al. Electromechanical Dyssynchrony Is Associated With Right Ventricular Remodeling and Dysfunction Independently of Pulmonary Regurgitation Late After Tetralogy of Fallot Repair. J Am Soc Echocardiogr. 2023;36(12):1315-23.
53. Zaidi A, Knight DS, Augustine DX, Harkness A, Oxborough D, Pearce K, et al. Echocardiographic assessment of the right heart in adults: a practical guideline from the British Society of Echocardiography. Echo Res Pract. 2020;7(1):G19-G41.
54. Weisstein EW. Curvature: Wolfram MathWorld; [Available from: https://mathworld.wolfram.com/Curvature.html.

Appendix 1: Literature review

Assessed as part of TM30003: Literature study.
Grade: 8.6

RV function and morphology assessment using 3D ultrasound in patients with Tetralogy of Fallot: a review.

Version 5 | 28-02-2024

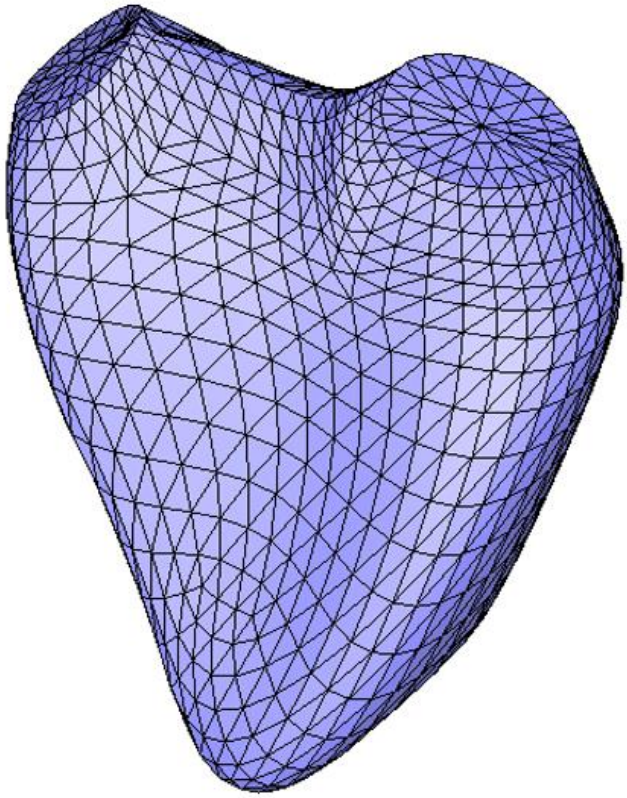

Literature Study – TM30003
04/12/2023 – 26/01/2024

J.W. (Jop) Schneijdenberg – MSc Technical Medicine student
NetID: 4677471
Email: J.W.Schneijdenberg@student.tudelft.nl

Medical supervisor:
Dr. A.E. (Annemien) van den Bosch – Associate Professor Cardiology/ Cardiologist
Email: A.E.vandenBosch@erasmusmc.nl
Technical supervisor:
Dr. ir. J.G. (Hans) Bosch – Associate Professor Thoraxcenter Biomedical Engineering
Email: J.Bosch@erasmusmc.nl
Daily supervisor:
R.R. (Rory) Zwaan, MSc – PhD candidate
Email: R.Zwaan@erasmusmc.nl

Abstract

Introduction: Tetralogy of Fallot (ToF) is commonly associated with right ventricle (RV) dilatation and subsequent RV dysfunction. Timely intervention can avoid complications, but requires close monitoring. Three-dimensional (3D) echocardiography could be a valuable modality for RV monitoring. This literature review will investigate what 3D echocardiography based parameters are most promising for functional and morphological RV assessment in ToF patients.

Background: Echocardiographic RV assessment is challenging due to its shape, complex contraction pattern, anatomical location and the limited field of view of echocardiography. 3D echocardiography overcomes several of these problems by visualizing the entire RV. From acquired images, 3D RV segmentations can be derived over time using image analysis software based on which morphological and functional 3D parameters can be obtained.

Investigational parameters: Five parameters were identified for the quantification of global RV function, consisting of global longitudinal strain, global circumferential strain, area strain, three-directional wall motion, and principal component analysis. For RV morphology quantification, three parameters were reported consisting of curvature, eccentricity, and sphericity.

Discussion and conclusion: Three-directional wall motion was identified as a comprehensive parameter for 3D echocardiography based evaluation of RV function in patients with ToF, allowing for multi-directional quantification of ventricular contraction. RV surface curvature is expected to be a valuable parameter for the quantification of RV, as the parameter can be calculated for any region on the RV surface. Using these parameters, follow-up of ToF patients may be improved and treatment timing could be optimized.

1. Introduction

1.1. Congenital heart disease

Congenital heart disease (CHD) represents a major global burden in child health (1, 2). With a prevalence of 9.4 per 1000 live births, more than a million babies are born with CHD each year (3). CHD has shown rising prevalence over the last decades. A possible cause is a higher detection rate as a result of diagnostic improvements, especially in developing countries (2, 3). Despite the rise in CHD prevalence, CHD caused mortality declined by 38.1% between 1990 and 2017 (4). Currently, 97% of patients born with CHD are expected to reach adulthood (5). This increase in survival is largely attributed to improvements in diagnostics, surgery, anesthesia, and postoperative care (6-9).

As a result of increased survival rates, the number of adult congenital heart disease (ACHD) patients has risen considerably over the past decades. These patients cope with high morbidity compared to the general population, consisting of early aging and significantly increased hospitalization rates due to cardiovascular events. Coronary syndrome, ischemic stroke, heart failure, and arrhythmia regularly occur in the ACHD population, requiring catheter intervention or surgery (10, 11). Besides the burden caused by disease existence, complications as a result of ACHD cause significant reduction in the quality of life of these patients (12). From an economical perspective, morbidity in ACHD patients increases healthcare costs due to hospitalization, surveillance, and pharmaceutical use, and gives high societal costs as a result of unemployment and absenteeism (13). To reduce the disease burden, adequate prevention and treatment of morbidity is vital, requiring life-long surveillance of ACHD patients in a specialized center (10).

1.2. Right ventricle

Whereas the left ventricle (LV) was usually subject of study due to its prominent role in acquired cardiovascular disease, the right ventricle (RV) received little scientific attention in the past. Due to the growing number of patients with ACHD, function of the RV has shown growing interest for treatment and prognosis (14). The RV is responsible for the pulmonary circulation in the body, pumping deoxygenated blood to the lungs. As the RV has another embryological origin as opposed to the LV, it shows a different response to altered loading conditions. As a result of its limited ability to adjust to alterations in loading, many ACHD patients develop disease related RV dysfunction, leading to morbidity and mortality (14, 15). Two potential causes of RV dysfunction in ACHD patients are volume overload and pressure overload of the RV. Volume overload can be the result of tricuspid regurgitation, pulmonary regurgitation, or shunting. These conditions cause increased blood flow into the RV, leading to RV enlargement and eventually RV failure. Examples of ACHD patients coping with volume overload are patients with Ebstein anomaly or an atrial septal defect (14, 16). Pressure overload may result from pulmonary stenosis. As a compensatory mechanism, RV pressure is increased to maintain RV function. This increased pressure requirement leads to myocardial hypertrophy, which will eventually cause RV failure. An example of ACHD patients coping with pressure overload are patients with congenital pulmonary stenosis (14, 17, 18).

1.3. Tetralogy of Fallot

Besides RV dysfunction caused by CHD, it may present as a result of surgical CHD repair. Tetralogy of Fallot (ToF) is the most common cyanotic CHD and commonly associated with RV dysfunction after surgical repair. With ToF, patients suffer from a combination of four cardiac

features: ventricular septal defect (VSD), RV outflow tract obstruction, overriding aorta, and RV hypertrophy (Figure 1A) (19). Surgical repair focuses on closing the VSD, after which LV flow is directed towards the aorta. Consequently, the RV outflow tract obstruction is reduced by infundibulectomy and pulmonary stenosis relief. Pulmonary stenosis relief is achieved through transannular patching and valvotomy (Figure 1B) (19, 20). Hereby, systemic and pulmonary flow are separated and unobstructed flow to the great arteries is assured. As a result of RV outflow tract surgery, repaired ToF patients are notorious for developing pulmonary regurgitation. These conditions lead to volume overload of the RV and are associated with RV dilatation and dysfunction (21, 22). Timely surgical pulmonary valve repair can avoid RV dysfunction related complications, such as atrial and ventricular arrhythmias, heart failure, and sudden cardiac death (23). To enable timely repair, close monitoring by trained adult congenital cardiologists is of paramount importance. Monitoring modalities include electrocardiography, transthoracic echocardiography, exercise testing, biomarker testing, and cardiac magnetic resonance imaging (24, 25). By separately analyzing regional RV function, long-term follow-up and timing of pulmonary valve repair may be further improved for patients with ToF (26).

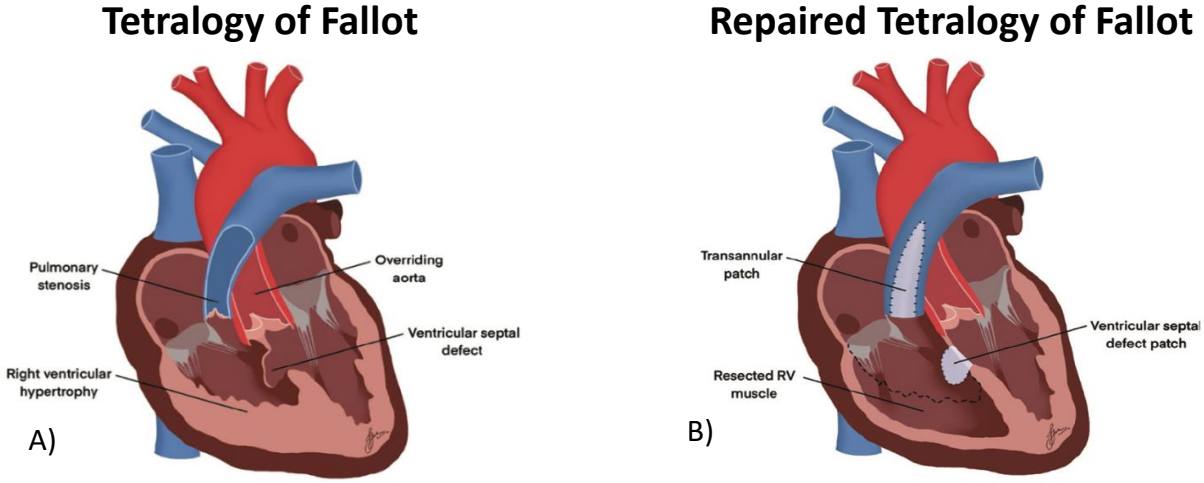

Figure 1: A) Heart with Tetralogy of Fallot, showing four features associated with the congenital heart disease. B) Heart after surgical repair of Tetralogy of Fallot, showing three performed repairs. Adaptation from Tale et al. (27)

1.4. Echocardiography

Echocardiography is the most commonly used, first-line imaging modality for diagnosis and follow-up of patients with ACHD. Its capabilities to assess cardiac morphology, physiology, pathophysiology, and function are essential for clinical management and prognosis of ACHD patients (28, 29). Though cardiac magnetic resonance imaging (cMRI) is also capable of assessing these cardiac characteristics, sometimes with even higher accuracy, echocardiography is preferred due to its real-time character, wide availability, portability, and lower expenses (30, 31). Current echocardiographic guidelines recommend a combination of RV dimension measurements and functional parameters for assessment of the RV. For these measurements, various ultrasound techniques are applied. Most morphological measurements are performed on brightness-mode (B-mode) two-dimensional (2D) slices of the RV. Motion-mode (M-mode), Doppler, and speckle tracking ultrasound imaging may be used for determining functional parameters (30). However, echocardiographic assessment of RV function and morphology proves to be more difficult than the assessment of LV parameters. Whereas the LV can be approximated as a conical shape, RV shape does not allow for such a symmetric geometrical assumption (14). The RV has a more complex crescent

shape, making the window on which measurements are performed crucial for their outcomes. With a lack of proper anatomical landmarks in the RV to determine standardized ultrasound windows, 2D measurements of the RV show large variations. As a result, inter-study comparison proves to be difficult for these measurements (30). Besides challenges caused by the complex RV morphology, thoracic positioning of the RV may complicate complete imaging of the ventricle. The RV is located far anteriorly and directly behind the sternum. As a result, the shadow of the sternum or lung tissue between the probe and the RV may obstruct the view of the lateral RV wall (29, 32).

Additionally, currently used functional parameters prove to be especially inadequate for patients suffering from ACHD. Regularly used functional parameters consist of the tricuspid annular plane systolic excursion (TAPSE) and tissue Doppler of the free lateral wall (S'). TAPSE is a measurement of excursion of the lateral tricuspid annulus between systole and diastole using M-mode ultrasound imaging. S' measures the longitudinal velocity of the tricuspid annular plane using tissue Doppler imaging. Both TAPSE and S' only represent longitudinal function of the basal part of the RV. Hence, an inaccurate representation is given of RV function as the RV outflow tract is not included in this measurement. The RV outflow tract plays a particularly vital role in many congenital deformations (32, 33).

A possible solution may be found in the use of three-dimensional (3D) echocardiography for functional and morphological measurements of the RV. With 3D echocardiography, limitations concerning windows and orientation are overcome by capturing the complete RV volume in one window, from which functional and morphological parameters can be determined. Additionally, accurate volume measurements and subsequently ejection fraction calculations are made possible using this 3D acquisition technique without the need for geometrical assumptions (30). As 3D echocardiography is increasingly finding its application in clinical practice, doors are opened for innovative and reproducible RV assessment techniques to further improve patient care. Recent research has investigated the applicability of 3D echocardiography for RV size, function, mechanics, and shape (34). However, no consensus has yet been reached on what 3D echocardiography parameters are most suitable for the assessment of RV function and morphology.

Therefore, this literature review will investigate what 3D echocardiography based parameters are most promising for functional and morphological RV assessment in patients with ToF. 3D echocardiography parameters will be identified from literature and weighed based on their ability to describe RV function and morphology of ToF patients.

2. Background

2.1. Echocardiography

Extrapolated from its use in flaw detection during metal production, cardiologist Inge Edler and physicist Carl Hellmuth Hertz first applied ultrasound for cardiac imaging in 1953. Starting with an amplitude mode (A-mode) signal capable of displaying depths of tissue interfaces, Edler and Hertz worked on a camera system to capture cardiac movement over time similar to M-mode ultrasound. They published their article "The Use of Ultrasonic Reflectoscope for the Continuous Recording of the Movements of Heart Walls" in 1954 (35), marking the beginning of many innovations in the field of echocardiography (36).

Over the past decades, echocardiography evolved from a one-dimensional to a 2D imaging modality, allowing for more accurate diagnosis and cardiac assessment. More recently, the field of 3D echocardiography is gaining popularity in clinical practice (37, 38). With advances in transducer technology, real-time 3D echocardiography can now be performed. Whereas the first 3D echocardiography images were acquired through tomographic scanning of a volume, matrix array transducers have been developed eliminating the need for mechanical movement to capture a volume (39).

A matrix array consists of a 2D array of transducer elements, rather than a single line of linearly positioned elements. By adding an additional dimension to the transducer, the ultrasound beam can be steered in multiple directions and not just in the transducer plane. Beam steering is achieved by exciting transducer elements at different times. The excitation of each element transmits an ultrasound wave. Through summation, the excitation of multiple adjacent elements brings about a wave front. By accurately delaying the excitation time of each transducer element, the wave front can be focused and steered to a desired location (Figure 2). As a result, a pyramidal volume scan can be obtained by steering the ultrasound beam in both lateral and elevation dimension, enabling the visualization of 3D structures (38, 39).

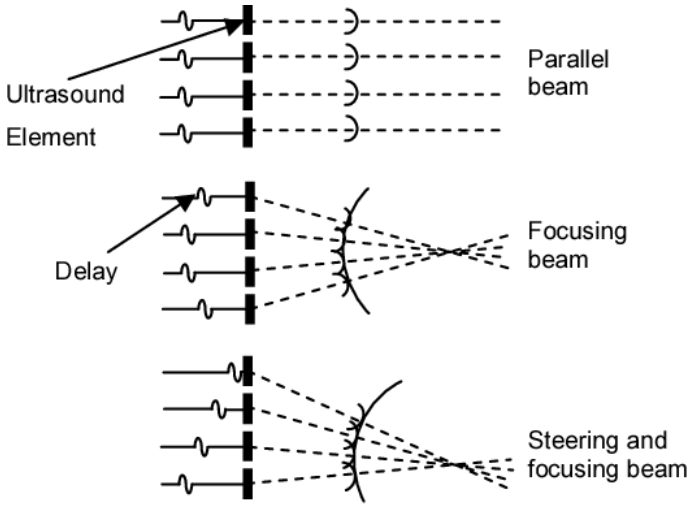

Figure 2: Schematic representation of two-dimensional beam steering and focusing by accurately tuning excitation times of each transducer element (40).

As an additional dimension must be scanned for the acquisition of a 3D ultrasound image, it takes more time to obtain a volume as opposed to a single slice. Consequently, 3D echocardiography is performed with a lower frame rate of 10 to 20 volumes per second than 2D echocardiography, capable of reaching 30 to 80 frames per second. This leads to a lower temporal resolution in 3D echocardiography. Therefore, fast moving cardiac structures may not be well visualized using 3D echocardiography (41). A method applied to increase temporal resolution is through decreasing spatial resolution or reducing the imaged volume. Thereby, less focus points require scanning enabling faster image acquisition. Another method to increase temporal resolution without making concessions in spatial resolution or volume is by using multiple-beat 3D echocardiography. This technique makes use of 3D acquisitions of partial cardiac volumes obtained during multiple heartbeats, after which the images are stitched together using the electrocardiogram (ECG). As a result, a single wide-view high resolution dataset is composed. A potential drawback of this technique is that stitching artefacts may be present in patients with an irregular heartbeat (42).

2.2. Echocardiography in the right ventricle

The echocardiographic assessment of the RV is challenging due to its shape, complex contraction pattern, anatomical location and the limited field of view of echocardiography. The RV has a crescent shape wrapped around the conical shape of the LV (Figure 3A). Because of this asymmetrical shape, no geometrical assumptions can be made based on selective 2D echocardiography. Therefore, the RV must be imaged using multiple windows to gain insight in its 3D shape, avoiding missing abnormalities or misjudging disease severity (30, 43). The complex shape of the RV can anatomically be subdivided into three components, consisting of the inlet, apical, and outlet part (Figure 3B). This subdivision is especially relevant in CHD patients, as malformations usually influence the functioning of one or more of these parts (22, 42). The unique shape of the healthy RV is essential for its ability to direct blood flow from the inlet to the outlet. As opposed to the LV, where inflow and outflow directions are nearly opposite, the RV flow path follows a gradual curve from inflow to outflow. As a result, there is no need for high pressure and RV walls are much thinner than LV walls. A change in RV shape, such as in CHD patients, therefore directly results in functional impairment (44). Therefore, each component part of the RV must be assessed thoroughly in RV echocardiography.

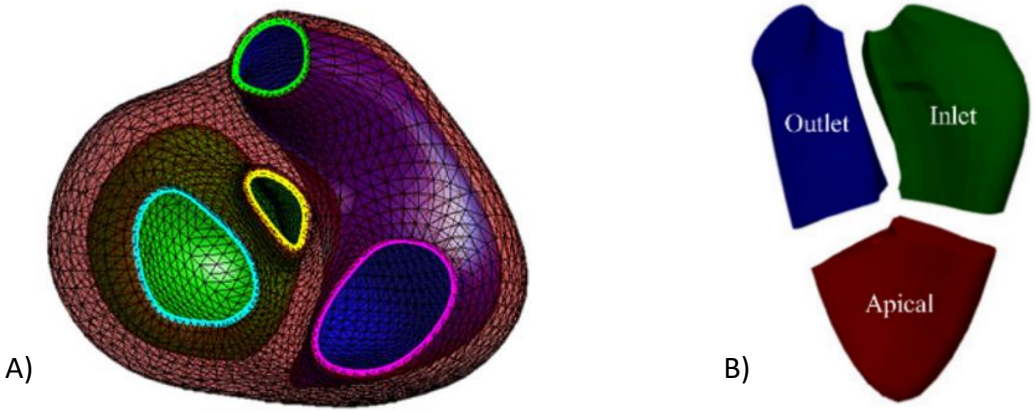

Figure 3: A) Model of the heart based on magnetic resonance imaging, showing the conical shape of the left ventricle in green and the crescent shape of the right ventricle in blue (45). B) Schematic of the right ventricle, subdivided into inlet, apical, and outlet components (46).

The complex contraction pattern of the RV has been described as peristaltic-like, starting at the RV inlet and ending at the outlet. RV myocardium is built up of two layers with different myofiber orientation. The outer epicardial layer consists of circumferentially oriented myofibers, whereas the subendocardial layer consists of myofibers oriented in longitudinal direction. This myocardial arrangement allows for multi-directional contraction. RV contraction can be subdivided into three main mechanisms. First, there is shortening in longitudinal direction by the subendocardial layer of myofibers. Likewise, there is circumferential contraction induced by the epicardial myofiber layer, which is also known as the bellows effect due to the inward movement of the RV free-wall. Lastly, shortening in anteroposterior direction is caused as an effect of LV contraction. LV contraction results in bulging of the ventricular septum into the RV cavum and stretching of the RV free-wall over the bulged septum. Together, these mechanisms generate RV pump function (47).

Besides shape and contraction pattern, the anatomical location of the RV introduces challenges for its echocardiographic assessment. The RV is the most anteriorly located part of the heart, situated directly behind the sternum and surrounded by lung tissue. As bone and

lung tissue poorly transmit ultrasound, image quality can be poor. Especially visualization of the RV outflow tract may be challenging in some patients as a result of the anatomical location of the RV (32). Lastly, it may be challenging to capture the entire RV in the field of view of one echocardiography window. The RV shows much movement during the cardiac cycle. As a result, it may be impossible to find a window in which both systolic and diastolic assessment of the RV is possible. Additionally, RV dilatation may cause RV size to increase severely, making it too large for one ultrasound window (30).

At present, European Society of Cardiology (ESC) echocardiography guidelines suggest the assessment of the RV by measuring RV size, RV systolic function, and RV diastolic function. However, accurately quantifying RV size based on 2D echocardiography is described as challenging due to suboptimal image quality, different ultrasound windows, or by the use of regional measurements. Measures for the quantification of RV systolic and diastolic function (TAPSE, S', FAC) are mostly angle dependent and do not represent global but rather regional RV function. Especially in patients following cardiac surgery, RV functional parameters based on 2D echocardiography poorly represent RV function (30).

2.3. Three-dimensional echocardiography

One major advantage of using 3D echocardiography is its application in RV volume and EF measurements. With 3D echocardiography, the entire RV volume is visualized, eliminating the need for geometric assumptions and potential inaccuracy as a result of foreshortening (37). However, a systematic underestimation of volume remains when comparing 3D echocardiography derived RV volumes with magnetic resonance imaging (MRI) derived RV volumes. This difference is caused by the difficulty to distinguish between endocardium and trabeculation as a result of lower resolution when imaging 3D volumes. Especially in patients with CHD causing RV dilatation, differences between echocardiography and MRI were big. Therefore, different reference values must be used when using RV volumes obtained from 3D echocardiography (48, 49). Besides the use of 3D echocardiography in RV volume and EF measurements, recent studies have investigated RV shape and functional analysis based on 3D echocardiography. Parameters such as curvature and strain were determined and associated with patient outcome. Additional parameters derived from 3D echocardiography are expected to aid future patient care (50).

Besides calculating parameters representing the global RV, it is possible to calculate regional parameters over an RV segment. Hereby, regional differences in RV function and morphology can be quantified. Different methods have been proposed for the subdivision of the RV into segments, but no golden standard had yet been defined (42, 51, 52). A consistent definition of RV regions is vital for the establishment of reference values, as differences in region definitions influence measurement outcomes.

In addition to RV parameters, 3D echocardiography is expected to greatly improve assessment and treatment planning of valvular heart disease. 3D echocardiography allows for the acquisition of dynamic images of valves, from a user-identified perspective. Hereby, heart valves can be visualized en face, enabling improved evaluation of valvular function by the sonographer. Besides, the en face view enables accurate reconstruction of valve annuli, to determine area, perimeter, dimensions, and eccentricity for better fitting of prosthetic valves (37, 53).

Current ESC echocardiography guidelines recommend the use of 3D echocardiography for assessment of RV size and function for diagnosis and prognosis in patients with CHD. Regional measurements for size can be replaced by the global measurement of volume, and ejection fraction (EF) can be calculated as measure for systolic RV function (42). Therefore, ESC guidelines on cardiac chamber quantification by echocardiography in adults recommend the use of RV volume and EF for RV size and function determination in laboratories with experience in 3D echocardiography (30).

2.4. Analysis software

3D RV segmentations can be derived over time from acquired RV 3D echocardiography images using semiautomatic image analysis software. A widely applied example of such software application is TomTec 4D RV-Function version 4.7 (Unterschleissheim, Germany) (54). As a first step, the 3D dataset must be aligned and several anatomical landmarks in both RV and LV are annotated in the end-diastolic frame. Longitudinal alignment is performed by drawing lines between the LV apex and the middle of the mitral annulus, and the RV apex and the middle of the tricuspid annulus in both four-chamber and two-chamber views. Consequently, the aortic annulus and the junction points between the RV wall and interventricular septum are identified. Lastly, a line must be drawn from the interventricular septum to the RV free wall, perpendicular to the midpoint of the interventricular septum (55, 56). Following these calibration steps, the software suggest an RV contouring and automatically identifies end-diastolic and end-systolic frames of the acquisition based on calculated volumes. Subsequently, the operator is allowed to perform manual adjustments to the automatic RV contouring in 4-chamber, coronal, and short axis views in both end-diastolic and end-systolic frames, after which the segmentation is rerun using speckle tracking to superimpose input delineations to other frames (Figure 4) (50, 54, 56). From ESC recommendations, consensus has been established on including trabeculae, papillary muscles, and the moderator band in the RV cavity delineations (30). Consecutively, a full 3D rendering of the cardiac chamber is available for all timeframes. This dynamic 3D endocardial surface rendering is known as a 'Beutel' (German for 'bag').

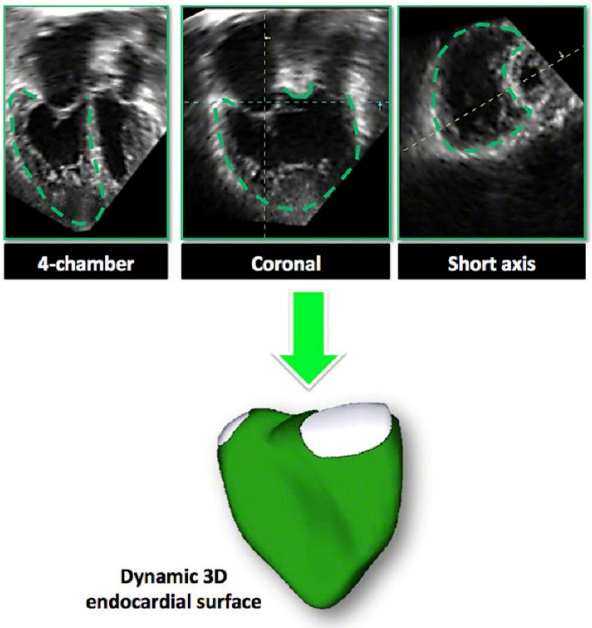

Figure 4: Schematic representation of the delineation and rendering of a right ventricle dynamic 3D surface. Manual adjustments were performed in 4-chamber, coronal, and short axis views in the end-diastolic and end-systolic frames, after which automatic 3D rendering is performed by TomTec 4D RV-Function software using endocardial surface tracking (50).

At this moment, TomTec 4D RV-Function software derives multiple parameters from input RV 3D echocardiography images. 3D parameters consist of RV end-diastolic volume (EDV), RV end-systolic volume (ESV), RV EF, and stroke volume (SV) (55-59). Besides 3D parameters, some 2D parameters are derived from the RV-focused apical 4-chamber view, consisting of RV longitudinal strain (LS), fractional area change (FAC), and tricuspid annulus longitudinal displacement (60).

Due to the semi-automatic character of the RV analysis software, outcomes depend on the input of the operator. Regularly, endocardial tracings performed automatically after input delineation require manual corrections by the operator. These manual adjustments introduce operator dependent variation (50). Nevertheless, earlier evaluation of the TomTec software found good, clinically acceptable inter- and intra-observer intraclass correlation coefficients (ICC) of > 0.9 for ventricular volumes and EF (56, 57). As a result of dependency on the experience and quality of the input delivered by the operator, ESC guidelines only recommend the use of 3D RV analysis for size and function assessment of the RV by experienced centers (30).

3. Investigational parameters

In addition to parameters currently available in TomTec 4D RV-Function software, research is being conducted after other parameters derived from 3D echocardiographic images of the RV capable of improving RV assessment. The PubMed database was searched to identify 3D echocardiography parameters for the quantification of RV function and morphology. Parameters based on color, spectral, or tissue Doppler echocardiography were not considered in this research.

3.1. RV function

To obtain an overview of parameters studied for the quantification of RV deformation, a PubMed search was performed using the search string: “Echocardiography, Three-dimensional”[Mesh] AND “Ventricular Function, Right”[Mesh] AND (“deformation”[tiab] OR “strain”[tiab]). Multiple 3D echocardiography based methods for RV deformation quantification were identified through this search or referenced articles. Deformation is commonly quantified as strain, which is defined as change in length of an object in a specific direction (Equation 1).

$$Strain\ (\%) = 100 * (L_t - L_0)/L_0$$

Equation 1: Calculation of strain as a percentage of the initial length of the object. L_t = length of object at time t; L_0 = initial length of object. Adaptation from Lang et al. (30).

A widely applied method for the assessment of RV deformation is through determination of RV longitudinal strain at the RV free wall and septum. Longitudinal strain is the fractional systolic cardiac chamber shortening in longitudinal direction (30). Using 3D rather than 2D echocardiography, foreshortening as a result of suboptimal ultrasound windows is prevented (61). Instead of calculating longitudinal strain at two predefined locations, another option is the measurement of 3D RV global longitudinal strain (GLS). 3D RV GLS is obtained by averaging longitudinal strain, measured in various segments all over the RV (Equation 2) (62). Calculating GLS from 3D echocardiographic images has proven to result in more accurate assessment of RV function in comparison to 2D echocardiography based longitudinal strain (57, 63). Research has proven decreased longitudinal strain in patients with cardiovascular disorders, such as pulmonary arterial hypertension and following heart transplantation (64, 65).

$$GLS\ (\%) = \frac{100}{n} * \sum_{j=1}^{n} \left(\frac{L_j^{end-systole}}{L_j^{end-diastole}} - 1 \right)$$

Equation 2: Calculation of global longitudinal strain (GLS) as a percentage of the initial length of the object over multiple right ventricle segments. GLS = global longitudinal strain; n = number of segments; $L_j^{end\text{-}systole}$ = length of segment j at end-systole; $L_j^{end\text{-}diastole}$ = length of segment j at end-diastole. Adaptation from Tokodi et al. (62).

Besides strain in longitudinal direction, multiple studies have looked at the role of circumferential strain in RV functioning. Circumferential strain is defined as regional percentage change of endocardial circumference (51). As for 3D GLS, 3D global circumferential strain (GCS) can be determined by averaging circumferential strain measured in various segments of the RV (Equation 3) (62). Though its contribution to RV function is smaller than that of longitudinal strain, decreased CS can be seen in specific RV segments in patients with CHD such as patients with ToF (66, 67). Moreover, Cho et al. identified decreased CS in the RV free wall as a response on RV afterload increase evoked by pulmonary artery banding (68). Moceri et al. confirmed this finding in ToF patients, where alterations in CS were mostly found in the RV free wall and the apical septum (69). Measuring regional changes in CS could therefore be of interest for regional RV function assessment.

$$GCS\ (\%) = \frac{100}{n} * \sum_{j=1}^{n} \left(\frac{C_j^{end-systole}}{C_j^{end-diastole}} - 1 \right)$$

Equation 3: Calculation of global circumferential strain (GCS) as a percentage of the initial circumference of the object over multiple right ventricle segments. GCS = global circumferential strain; n = number of segments; $C_j^{end\text{-}systole}$ = circumference of segment j at end-systole; $C_j^{end\text{-}diastole}$ = circumference of segment j at end-diastole. Adaptation from Tokodi et al. (62).

In addition to unidirectional strain, a parameter has been constructed to express area strain. Area strain is defined as the percentage change of RV segment area during systole, which can be seen as a product of longitudinal and circumferential strain components (Equation 4). Ishizu et al. found that differences in segmental deformation of the RV wall influenced RV function in patients with structural heart disease. Especially diminished RV inlet area strain correlated significantly with deteriorated RV EF (51). Moreover, Moceri et al. found decreased area strain in the RV free wall and apical septum in a 3D echocardiography study of 28 ToF patients (69). Atsumi et al. investigated a parameter comparable to area strain, called area change ratio (ACR), in patients suffering from pulmonary arterial hypertension (PAH). They found intersegment differences in ACR, dependent on the level of pressure overload during stress. ACR was suggested as a potentially robust parameter for regional abnormality detection, capable of representing underlying RV mechanics (70).

$$AS\ (\%) = 100 * \left(\frac{A^{end-systole}}{A^{end-diastole}} - 1 \right)$$

Equation 4: Calculation of area strain (AS) as a percentage of the initial segmental area of the object. AS = area strain; $A^{end\text{-}systole}$ = area of segment at end-systole; $A^{end\text{-}diastole}$ = area of segment at end-diastole. Adaptation from Tokodi et al. (62).

Additionally, studies have been looking at RV wall motion in lateral, radial and anteroposterior direction for the assessment of RV deformation (Figure 5). By determining shortening in all three directions of RV wall motion, their partial contribution to EF can be calculated (71). Research has shown differences in dominant directions of wall motion, influenced by the presence of cardiac disorders (72). For example, ToF patients were found to have significantly lower longitudinal shortening contribution to RV EF, whilst maintaining radial and anteroposterior motion (67). These findings show the potential added value of measuring RV wall motion in three directions, gaining more thorough insight in RV function of CHD patients.

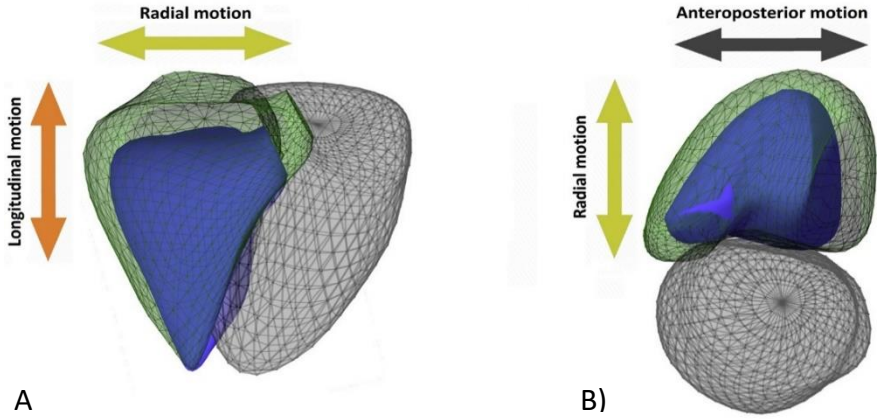

Figure 5: Right ventricle wall motion broken down into three separate directions: longitudinal, radial, and anteroposterior. Green: end-diastolic right ventricular volume; blue: end-systolic right ventricular volume; gray: left ventricle. A) anterior view of the right ventricle, showing motion in the longitudinal and radial direction. B) superior view of the right ventricle, showing motion in the radial and anteroposterior direction. Adaptation from Lakatos et al. (73).

Lastly, research groups have been reporting on the use of principal component analysis (PCA) for functional assessment of the RV. Most of above mentioned methods for strain quantification focus on RV motion in a specific direction. As a result, these parameters do not allow for effective quantification of multidirectional sliding motion, also known as shear. This may lead to an underestimation of RV contraction. PCA calculates the two dominant strain component vectors of a tissue patch. Primary principal strain (PS) is defined in the direction in which most shortening occurs and secondary PS is defined in the direction perpendicular to primary PS. Subsequently, each deformation of the object can be expressed as a combination of primary and secondary PS together with a magnitude for these components, which bypasses the need to separately quantify shear (74, 75). Research performed by Sato et al. used 3D speckle-tracking based 4D LV-analysis software from TomTec for the analysis of RV's of patients with hypoplastic left heart syndrome after Fontan palliation. Due to RV remodeling in these patients, LV software could be applied. This research compared longitudinal strain, circumferential strain, and principal strain and showed highest strains in PS measurements with strong correlation between PS and RV EF (74). Satriano et al. looked at principal strain in patients with PAH using 4D RV-function software from TomTec. Their research revealed significantly lower PS with significantly smaller contraction angle in PAH patients in comparison with healthy controls (75). The results of PCA analysis resemble those of AS, except for the fact that shear strains are not taken into account in AS. Therefore, RV mechanics can more easily be understood for the assessment of functional changes by using PS, as the primary direction of RV contraction is quantified and not only axis dependent strains are taken into account when performing PCA (74).

3.2. RV morphology

Parameters available for quantitative RV shape assessment based on 3D echocardiography were investigated through a PubMed search using the search string: "Echocardiography, Three-dimensional"[Mesh] AND "Ventricular Function, Right"[Mesh] AND "shape"[tiab]. From articles found in this search or referenced articles, multiple methods for RV shape quantification were identified.

The RV shape parameter mostly reported in literature is curvature of the endocardial surface. Curvature of a surface is defined as the inverse of the radius of the circle best approximating the surface curvature (Equation 5) (50, 76).

$$k\ [m^{-1}] = \frac{1}{R}$$

Equation 5: Calculation of curvature. K = curvature; R = radius of circle best approximating the surface curvature. Adaptation from Addetia et al. (50).

3D echocardiography derived curvature was first reported by Addetia et al. for the assessment of RV shape in patients with PAH (50). For the calculation of RV curvature, the dynamic 3D endocardial RV surface was exported from TomTec as a connected mesh file. Local curvature was determined for each point in the mesh by fitting two orthogonal circles on the RV surface surrounding the mesh point. Local curvature was calculated by calculating mean curvature of the orthogonal circles (Equation 6), after which curvature values were normalized (Equation 7) and averaged per RV segment to obtain regional 3D curvature (50, 76).

$$K\ [m^{-1}] = \frac{k_1 + k_2}{2}$$

Equation 6: Calculation of local curvature by calculating mean curvature of orthogonal circles . K = local curvature; k_1 = curvature of first orthogonal circle approximating the surface curvature; k_1 = curvature of second orthogonal circle approximating the surface curvature. Adaptation from Addetia et al. (50).

$$K_{reg}\ [m^{-1}] = \sqrt[3]{\frac{4\pi}{3V_{reg}}}$$

$$K_n\ [m^{-1}] = \frac{K}{K_{reg}}$$

Equation 7: Calculation of normalized curvature by dividing by regional curvature. K_{reg} = regional curvature; V_{reg} = regional volume; K_n = normalized curvature; K = local curvature. Adaptation from Addetia et al. (50).

RV endocardial surface curvature is described from a perspective looking at the surface from the outside of the ventricle. A flat surface is expressed as a curvature of 0, a concave surface has a curvature of < 0, and a convex surface as a curvature of >0 (77). A schematic representation of curvature calculation steps and various curvatures can be seen in Figure 6.

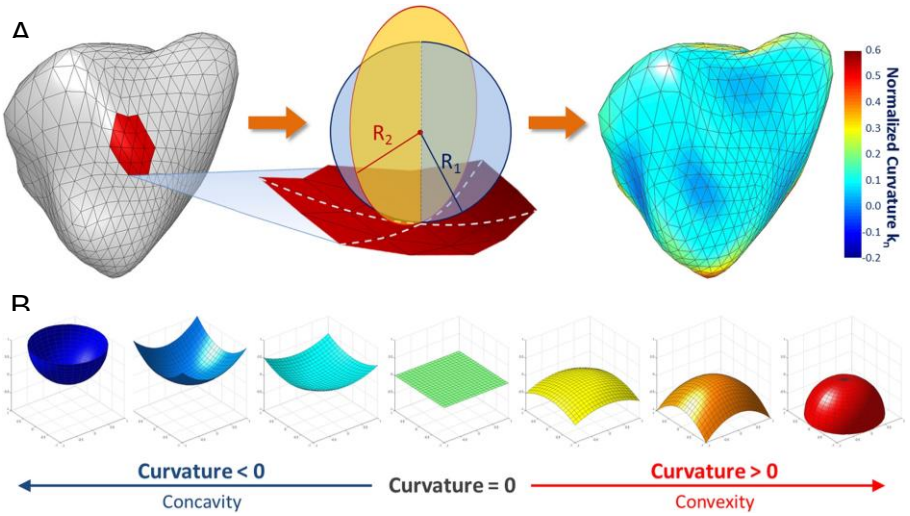

Figure 6: Schematic representation of curvature calculation steps and various curvatures. A) A local neighborhood surrounding a single mesh point is considered (red, left image). Two orthogonal circles (blue and yellow, middle image) are fitted to best match the local surface. From these fitted circles, a local curvature can be calculated. Curvature is calculated for each mesh point and superimposed on the RV surface (right image). B) Different values of curvature, ranging from <0 (concave) to 0 (flat) to >0 convex (50).

Analyses of regional RV endocardial surface curvature in patients with PAH performed by Addetia et al. revealed a more convex RV outflow tract and septum in comparison with controls. Additionally, RV free-wall segments remained equally convex throughout the entire cardiac cycle in PAH patients, whereas controls showed a decrease of convexity towards systole (50). Bidviene et al. investigated regional RV wall curvature in patients with pressure and volume overload of the RV. The volume overload group consisted of repaired ToF patients and the pressure overload group consisted of patients suffering from pulmonary hypertension (PH). In line with findings of Addetia et al, both patient groups showed less convex RV free-wall segments and more convex RV outflow tract and septum than controls. It was also found that more convexity of the RV outflow tract at systole resulted in worse RV systolic function. Additionally, ToF patients showed less convexity of the RV septum in diastole, whereas PH patients showed more RV septum convexity during systole (78). Moceri et al. compared RV curvature of two patient groups with volume overload disorders, ToF and atrial septal defect (ASD) patients. The authors found no differences in RV curvature between patients with volume overload caused by ToF or by ASD (69). From these studies, it was concluded that 3D curvature analysis can aid in the quantification of RV remodeling patterns of the entire endocardial surface to improve understanding of RV shape and function in various diseases (50, 69).

A study performed by Leary et al. reported on the use of eccentricity as parameter for the assessment of RV shape (79). Eccentricity is defined as a ratio between area and perimeter of a short-axis RV cross-section (Figure 7A), expressed as a number ranging from 1 to 0, representing a circle or a line respectively (Equation 8) (80).

$$e = \frac{4\pi A}{C^2}$$

Equation 8: Calculation of eccentricity. e = eccentricity; A = cross-sectional area of the RV; C = circumference of the RV cross-section. Adaptation from Gibson et al. (80).

This research compared RV eccentricity of PH patients with controls, and found increased eccentricity in all RV segments of PH patients and decreased RV function (79). Sheehan et al. studied RV eccentricity in ToF patients and found significantly increased eccentricity in the apical segments of the RV. This apical dilatation was potentially caused by myocardial thinning, and could be a contributing factor to tricuspid regurgitation (81).

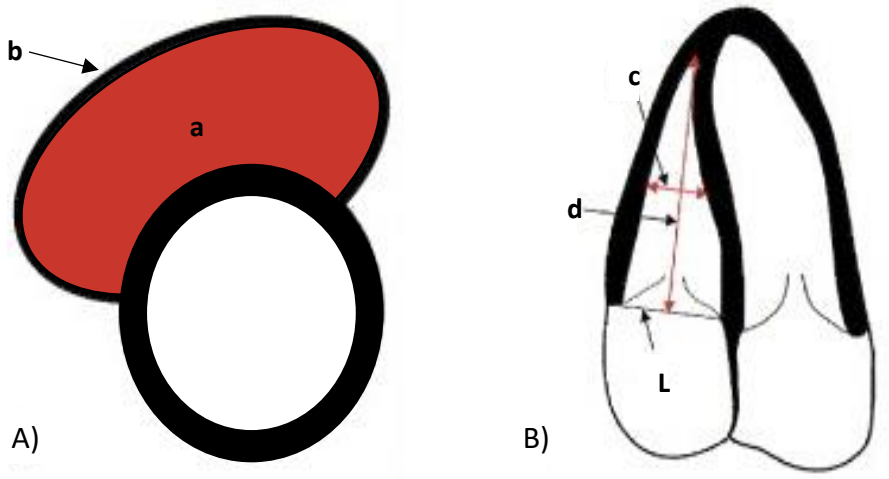

Figure 7: Schematic representation of the calculation of A) eccentricity (short axis view) and b) sphericity (four-chamber view). a = cross-sectional area of the RV; b = circumference of RV cross-section; c = distance between right ventricle free-wall and septum; d = length between apex and middle of line L; L = tricuspid annular plane. Adaptation from Kim et al. (82).

A parameter somewhat similar to eccentricity is sphericity. This parameter also quantifies roundness of the RV, only from four-chamber rather than short-axis perspective (Figure 7B). Grapsa et al. analyzed sphericity in PAH patients, and defined sphericity as the ratio between the short-axis and long axis of the RV at end-diastole. They found higher sphericity in PAH patients compared with controls, and degree of RV sphericity had predictive value for clinical deterioration of PAH patients. However, right atrial sphericity had even higher predictive value than RV sphericity and was therefore recommended as measure for the prediction of clinical deterioration (83). Kim et al. looked whether a correlation could be found between RV sphericity and degree of functional tricuspid regurgitation. This research concluded that mild, moderate, and severe functional tricuspid regurgitation could not be differentiated based on RV sphericity (82).

4. Discussion

In this literature review, the main challenges encountered during the echocardiographic assessment of the RV were identified as the multidimensional contraction pattern, non-geometrical shape, and difficult anatomical location of the RV, and the limited field of view of echocardiography. As a result, RV function and morphology are difficult to quantify using 2D imaging. 3D echocardiography could overcome several of these issues. For effective implementation of 3D echocardiography for RV assessment, novel parameters need to be identified.

Investigational 3D echocardiography parameters could be used for improved follow-up of patients with ToF. These patients are known to develop RV dilatation and subsequent RV dysfunction as a result of pulmonary valve regurgitation (22). RV dysfunction is a functional RV characteristic that expresses itself as compromised contraction, most evident in the longitudinal direction. In response, contraction in circumferential direction is enhanced in these patients (67). Quantification of these contraction patterns could improve understanding of the mechanism behind RV dysfunction and improve clinical decision making. RV dilatation is a morphological characteristic of the RV. Research found different RV regions with increased rounding in ToF patients, especially around the septum, RV outflow tract, and apical segment, reflecting possible functional impairment (78, 81). To prevent irreversible RV remodeling, the investigational parameters should aim to quantify functional and morphological changes of the RV to improve echocardiographic follow-up of ToF patients and enable optimal treatment timing.

4.1. Findings

This literature review investigated what 3D echocardiography based parameters are most promising for functional and morphological RV assessment in patients with ToF. Five parameters were identified from literature for the quantification of global RV function, consisting of GLS, GCS, AS, three-directional wall motion, and PCA. For RV morphology quantification, three parameters were reported in literature consisting of curvature, eccentricity, and sphericity. Besides reporting global function or morphology, each of these parameters could be reported per region or segment of the RV to gain insight in segmental differences.

Due to the experimental nature in which most 3D echocardiographic parameters have been investigated, consensus has not yet been reached on what parameter is most promising for

the quantification of RV function and morphology. Earlier research on the validation of echocardiographic parameters by Zandstra et al. suggested three criteria by which parameter usefulness could be weighed: feasibility to obtain in clinical practice, correlation with golden standard measurements, and measurement reliability (84).

The parameters identified for the quantification of RV function consisted of both unidimensional and multidimensional parameters. RV function parameters allowing for the quantification of multidimensional deformation consist of AS, three-directional wall motion, and PCA. GLS and GCS quantify RV function in one specified direction, longitudinal or circumferential direction respectively. Since ToF patients were found to have regionally altered contraction patterns in various directions, the use of a multidimensional parameter is preferred for the quantification of RV function. Looking at the found multidimensional parameters, AS was identified as a robust parameter for the identification of regional differences in RV mechanics. The parameter could be obtained automatically from 3D echocardiography images, and intra- and inter-observer variability were reported as excellent (62). However, only AS of the RV inlet could be correlated to the golden standard MRI-derived RV EF (51). Moreover, identifying altered AS does not provide the physician with any information on what component of contraction is impaired or augmented in the patient, especially limiting the diagnostic value of AS for ToF patients where specific contraction components are altered. As opposed to AS, three-directional wall motion is a method which quantifies RV wall motion in longitudinal, radial, and anteroposterior direction separately. Specific directions of wall motion were found to be affected in different cardiac disorders, by which the parameter could improve understanding of disease specific pathophysiology (67, 72, 73). Unfortunately, correlation with golden standard MRI and intra- and inter-observer variability have not yet been reported for this parameter. Lastly, PCA was identified as a method for the assessment of multidimensional RV function. In this parameter, both stress and shear are included, giving a complete representation of RV function. PCA was not compared to golden standard MRI imaging in these investigations, but good inter- and intra-observer variabilities were found (74, 75). PCA is a relatively new method in the field of echocardiography, as a result of which thorough understanding of the parameter must be established by the physician before implementation is feasible. No studies on its usability on ToF patients has been performed so far, but its capabilities may be able to shed new light on RV pathophysiology.

Using either the three-directional wall motion or the PCA method, a comprehensive analysis of RV function in patients with ToF can be performed. Both methods may be capable of exposing underlying mechanisms of RV failure by breaking down RV contraction in multiple directions. Considering the novelty of PCA in echocardiography, three-directional wall motion analysis is expected to allow for easier clinical implementation as a result of its resemblance with other strain related parameters in current clinical practice.

Parameters for the quantification of RV morphology reported in literature are curvature, eccentricity, and sphericity. Eccentricity and sphericity evaluate RV shape from 2D cross-sections obtained from a 3D volume, whereas curvature considers the relation between one point on the RV surface and neighboring points in the 3D surface around it. Therefore, eccentricity and sphericity can only be determined in different regions along one axis of the RV, whereas curvature can be determined in any region defined on the RV surface. With

research especially reporting morphological changes around the RV interventricular septum and RV outflow tract, curvature will be able to provide a more comprehensive analysis of RV shape than eccentricity and sphericity (78). 3D echocardiography derived curvature values have not yet been compared to golden standard MRI measurements in literature. Addetia et al. did find good inter- and intra-observer variability for curvature (50).

RV surface curvature is expected to be a valuable parameter for the quantification of RV morphology both regionally and globally. By being able to calculate curvature of any segment of the RV surface, new insights can be gained in morphological changes occurring in patients with ToF and their effects on RV function. Through improved monitoring of RV morphology, patient follow-up may be improved and timing of interventions could be optimized.

4.2. Future directions

Following the outcomes of this literature review, additional research is required to investigate the added value of three-directional wall motion for RV function assessment and curvature for RV morphology assessment in patients with ToF. Three-directional wall motion and curvature will be obtained from dynamic 3D endocardial surface renderings, after which analyses can be performed to evaluate their added value in the follow-up of ToF patients. Besides the investigation of global parameters, this review showed interesting regional differences in RV function and morphology. Subdivisions of the RV into regions differed between articles. Therefore, additional research is required to investigate what regional subdivision is most suited for the proposed parameters. Additionally, all proposed parameters will have to be assessed based on their feasibility, reliability, and clinical relevance before clinical implementation is feasible.

4.3. Limitations

For this literature review, the PubMed database was searched for articles on echocardiographic parameters for RV function and morphology quantification. Not all articles published on these topics may have been identified, as no systematic search was performed and only the PubMed database was examined. Furthermore, quantitatively comparing parameters identified from literature was impossible as a result of the investigative nature in which the parameters were researched. This resulted in a wide variety in outcome measures. Therefore, no meta-analysis could be performed and parameters could not be weighed quantitatively. Additionally, this review was limited to echocardiography parameters, excluding Doppler echocardiography. Usable parameters may have been identified in other imaging modalities of which the use could be extrapolated to application in echocardiography.

5. Conclusion

From this literature review, three-directional wall motion was identified as a comprehensive parameter for 3D echocardiography based evaluation of RV function in patients with ToF. This parameter allows for multi-directional quantification of ventricular contraction. RV surface curvature is expected to be a valuable parameter for the quantification of RV morphology both regionally and globally, as the parameter can be calculated for any region on the RV surface. Additional research is required to investigate the added value of three-directional wall motion for the assessment of RV function and curvature for the assessment of RV morphology in patients with ToF. The use these novel 3D echocardiography based parameters may improve follow-up and optimize treatment timing for ToF patients.

References

1. van der Linde D, Konings EE, Slager MA, Witsenburg M, Helbing WA, Takkenberg JJ, et al. Birth prevalence of congenital heart disease worldwide: a systematic review and meta-analysis. J Am Coll Cardiol. 2011;58(21):2241-7.
2. Collaborators GBDCHD. Global, regional, and national burden of congenital heart disease, 1990-2017: a systematic analysis for the Global Burden of Disease Study 2017. Lancet Child Adolesc Health. 2020;4(3):185-200.
3. Liu Y, Chen S, Zühlke L, Black GC, Choy MK, Li N, et al. Global birth prevalence of congenital heart defects 1970-2017: updated systematic review and meta-analysis of 260 studies. Int J Epidemiol. 2019;48(2):455-63.
4. Wu W, He J, Shao X. Incidence and mortality trend of congenital heart disease at the global, regional, and national level, 1990-2017. Medicine (Baltimore). 2020;99(23):e20593.
5. Mandalenakis Z, Giang KW, Eriksson P, Liden H, Synnergren M, Wåhlander H, et al. Survival in Children With Congenital Heart Disease: Have We Reached a Peak at 97%? J Am Heart Assoc. 2020;9(22):e017704.
6. Lopez KN, Morris SA, Sexson Tejtel SK, Espaillat A, Salemi JL. US Mortality Attributable to Congenital Heart Disease Across the Lifespan From 1999 Through 2017 Exposes Persistent Racial/Ethnic Disparities. Circulation. 2020;142(12):1132-47.
7. Boneva RS, Botto LD, Moore CA, Yang Q, Correa A, Erickson JD. Mortality associated with congenital heart defects in the United States: trends and racial disparities, 1979-1997. Circulation. 2001;103(19):2376-81.
8. Erikssen G, Liestøl K, Seem E, Birkeland S, Saatvedt KJ, Hoel TN, et al. Achievements in congenital heart defect surgery: a prospective, 40-year study of 7038 patients. Circulation. 2015;131(4):337-46; discussion 46.
9. Moons P, Bovijn L, Budts W, Belmans A, Gewillig M. Temporal trends in survival to adulthood among patients born with congenital heart disease from 1970 to 1992 in Belgium. Circulation. 2010;122(22):2264-72.
10. Müller MJ, Norozi K, Caroline J, Sedlak N, Bock J, Paul T, et al. Morbidity and mortality in adults with congenital heart defects in the third and fourth life decade. Clin Res Cardiol. 2022;111(8):900-11.
11. Saha P, Potiny P, Rigdon J, Morello M, Tcheandjieu C, Romfh A, et al. Substantial Cardiovascular Morbidity in Adults With Lower-Complexity Congenital Heart Disease. Circulation. 2019;139(16):1889-99.
12. Khajali Z, Sayyadi A, Ansari Z, Aliramezany M. Quality of life in adult patients with congenital heart disease: Results of a double-center study. Front Psychiatry. 2022;13:1062386.
13. Willems R, Ombelet F, Goossens E, De Groote K, Budts W, Moniotte S, et al. Long-term healthcare utilization, medical cost, and societal cost in adult congenital heart disease. Congenital Heart Disease. 2020;15(6):399-429.
14. Davlouros PA, Niwa K, Webb G, Gatzoulis MA. The right ventricle in congenital heart disease. Heart. 2006;92 Suppl 1(Suppl 1):i27-38.
15. Kaufman BD, Desai M, Reddy S, Osorio JC, Chen JM, Mosca RS, et al. Genomic profiling of left and right ventricular hypertrophy in congenital heart disease. J Card Fail. 2008;14(9):760-7.
16. Bleeker GB, Steendijk P, Holman ER, Yu CM, Breithardt OA, Kaandorp TA, et al. Acquired right ventricular dysfunction. Heart. 2006;92 Suppl 1(Suppl 1):i14-8.

17. Ruckdeschel E, Kim YY. Pulmonary valve stenosis in the adult patient: pathophysiology, diagnosis and management. Heart. 2019;105(5):414-22.
18. Marchini F, Meossi S, Passarini G, Campo G, Pavasini R. Pulmonary Valve Stenosis: From Diagnosis to Current Management Techniques and Future Prospects. Vasc Health Risk Manag. 2023;19:379-90.
19. Wilson R, Ross O, Griksaitis MJ. Tetralogy of Fallot. BJA Educ. 2019;19(11):362-9.
20. Mainwaring RD, Hanley FL. Tetralogy of Fallot Repair: How I Teach It. Ann Thorac Surg. 2016;102(6):1776-81.
21. Mahle WT, Parks WJ, Fyfe DA, Sallee D. Tricuspid regurgitation in patients with repaired Tetralogy of Fallot and its relation to right ventricular dilatation. Am J Cardiol. 2003;92(5):643-5.
22. Giannopoulos NM, Chatzis AC, Bobos DP, Kirvassilis GV, Tsoutsinos A, Sarris GE. Tetralogy of Fallot: influence of right ventricular outflow tract reconstruction on late outcome. Int J Cardiol. 2004;97 Suppl 1:87-90.
23. Bouzas B, Kilner PJ, Gatzoulis MA. Pulmonary regurgitation: not a benign lesion. Eur Heart J. 2005;26(5):433-9.
24. Ammash NM, Dearani JA, Burkhart HM, Connolly HM. Pulmonary regurgitation after tetralogy of Fallot repair: clinical features, sequelae, and timing of pulmonary valve replacement. Congenit Heart Dis. 2007;2(6):386-403.
25. Rodriguez-Serrano M, Rueda J, Buendía F, Monto F, Aguero J, Osa A, et al. β2-Adrenoceptors and GRK2 as Potential Biomarkers in Patients With Chronic Pulmonary Regurgitation. Front Pharmacol. 2019;10:93.
26. Bove T, Vandekerckhove K, Devos D, Panzer J, De Groote K, De Wilde H, et al. Functional analysis of the anatomical right ventricular components: should assessment of right ventricular function after repair of tetralogy of Fallot be refined? Eur J Cardiothorac Surg. 2014;45(2):e6-12.
27. Tale E, Nikakis J, Malkov D, Arora US, Jose J, Cohen TJ. A 58-Year Follow-up of Complete Surgical Correction of Tetralogy of Fallot: A Marvel of Modern Medicine. EP Lab Digest. 2022;22(7).
28. Li W, West C, McGhie J, van den Bosch AE, Babu-Narayan SV, Meijboom F, et al. Consensus recommendations for echocardiography in adults with congenital heart defects from the International Society of Adult Congenital Heart Disease (ISACHD). Int J Cardiol. 2018;272:77-83.
29. Baumgartner H, De Backer J, Babu-Narayan SV, Budts W, Chessa M, Diller GP, et al. 2020 ESC Guidelines for the management of adult congenital heart disease. Eur Heart J. 2021;42(6):563-645.
30. Lang RM, Badano LP, Mor-Avi V, Afilalo J, Armstrong A, Ernande L, et al. Recommendations for cardiac chamber quantification by echocardiography in adults: an update from the American Society of Echocardiography and the European Association of Cardiovascular Imaging. J Am Soc Echocardiogr. 2015;28(1):1-39 e14.
31. Gardner BI, Bingham SE, Allen MR, Blatter DD, Anderson JL. Cardiac magnetic resonance versus transthoracic echocardiography for the assessment of cardiac volumes and regional function after myocardial infarction: an intrasubject comparison using simultaneous intrasubject recordings. Cardiovasc Ultrasound. 2009;7:38.
32. Zaidi A, Knight DS, Augustine DX, Harkness A, Oxborough D, Pearce K, et al. Echocardiographic assessment of the right heart in adults: a practical guideline from the British Society of Echocardiography. Echo Res Pract. 2020;7(1):G19-G41.

33. Schneider M, Binder T. Echocardiographic evaluation of the right heart. Wien Klin Wochenschr. 2018;130(13-14):413-20.
34. Surkova E, Muraru D, Iliceto S, Badano LP. The use of multimodality cardiovascular imaging to assess right ventricular size and function. Int J Cardiol. 2016;214:54-69.
35. Edler I, Hertz CH. The use of ultrasonic reflectoscope for the continuous recording of the movements of heart walls. 1954. Clin Physiol Funct Imaging. 2004;24(3):118-36.
36. Edler I, Lindström K. The history of echocardiography. Ultrasound Med Biol. 2004;30(12):1565-644.
37. Lang RM, Addetia K, Narang A, Mor-Avi V. 3-Dimensional Echocardiography: Latest Developments and Future Directions. JACC Cardiovasc Imaging. 2018;11(12):1854-78.
38. von Ramm OT, Smith SW. Real time volumetric ultrasound imaging system. J Digit Imaging. 1990;3(4):261-6.
39. Smith NB, Webb A. Introduction to Medical Imaging: Physics, Engineering and Clinical Applications: Cambridge University Press; 2010.
40. Tan MT, Chu CM, Chauhan S. High intensity ultrasound phased array for surgical applications. 2006 International Conference on Biomedical and Pharmaceutical Engineering. 2006:564-8.
41. Jalilian H, Afrakhteh S, Iacca G, Demi L. Increasing frame rate of echocardiography based on a novel 2D spatio-temporal meshless interpolation. Ultrasonics. 2023;131:106953.
42. Lang RM, Badano LP, Tsang W, Adams DH, Agricola E, Buck T, et al. EAE/ASE recommendations for image acquisition and display using three-dimensional echocardiography. J Am Soc Echocardiogr. 2012;25(1):3-46.
43. Ho SY, Nihoyannopoulos P. Anatomy, echocardiography, and normal right ventricular dimensions. Heart. 2006;92 Suppl 1(Suppl 1):i2-13.
44. Fredriksson AG, Zajac J, Eriksson J, Dyverfeldt P, Bolger AF, Ebbers T, et al. 4-D blood flow in the human right ventricle. Am J Physiol Heart Circ Physiol. 2011;301(6):H2344-50.
45. Mauger C, Gilbert K, Lee AM, Sanghvi MM, Aung N, Fung K, et al. Right ventricular shape and function: cardiovascular magnetic resonance reference morphology and biventricular risk factor morphometrics in UK Biobank. Journal of Cardiovascular Magnetic Resonance. 2019;21(1):41.
46. Hodzic A, Bernardino G, Legallois D, Gendron P, Langet H, De Craene M, et al. Right Ventricular Global and Regional Remodeling in American-Style Football Athletes: A Longitudinal 3D Echocardiographic Study. Applied Sciences. 2021;11(8):3357.
47. Kovács A, Lakatos B, Tokodi M, Merkely B. Right ventricular mechanical pattern in health and disease: beyond longitudinal shortening. Heart Fail Rev. 2019;24(4):511-20.
48. Crean AM, Maredia N, Ballard G, Menezes R, Wharton G, Forster J, et al. 3D Echo systematically underestimates right ventricular volumes compared to cardiovascular magnetic resonance in adult congenital heart disease patients with moderate or severe RV dilatation. J Cardiovasc Magn Reson. 2011;13(1):78.
49. Greiner S, André F, Heimisch M, Aurich M, Steen H, Katus HA, et al. A closer look at right ventricular 3D volume quantification by transthoracic echocardiography and cardiac MRI. Clin Radiol. 2019;74(6):490 e7- e14.
50. Addetia K, Maffessanti F, Yamat M, Weinert L, Narang A, Freed BH, et al. Three-dimensional echocardiography-based analysis of right ventricular shape in pulmonary arterial hypertension. Eur Heart J Cardiovasc Imaging. 2016;17(5):564-75.

51. Ishizu T, Seo Y, Atsumi A, Tanaka YO, Yamamoto M, Machino-Ohtsuka T, et al. Global and Regional Right Ventricular Function Assessed by Novel Three-Dimensional Speckle-Tracking Echocardiography. J Am Soc Echocardiogr. 2017;30(12):1203-13.
52. Yu HK, Li SJ, Ip JJ, Lam WW, Wong SJ, Cheung YF. Right ventricular mechanics in adults after surgical repair of tetralogy of fallot: insights from three-dimensional speckle-tracking echocardiography. J Am Soc Echocardiogr. 2014;27(4):423-9.
53. Jilaihawi H, Doctor N, Kashif M, Chakravarty T, Rafique A, Makar M, et al. Aortic annular sizing for transcatheter aortic valve replacement using cross-sectional 3-dimensional transesophageal echocardiography. J Am Coll Cardiol. 2013;61(9):908-16.
54. Sciancalepore MA, Maffessanti F, Patel AR, Gomberg-Maitland M, Chandra S, Freed BH, et al. Three-dimensional analysis of interventricular septal curvature from cardiac magnetic resonance images for the evaluation of patients with pulmonary hypertension. Int J Cardiovasc Imaging. 2012;28(5):1073-85.
55. Muraru D, Badano LP, Nagata Y, Surkova E, Nabeshima Y, Genovese D, et al. Development and prognostic validation of partition values to grade right ventricular dysfunction severity using 3D echocardiography. Eur Heart J Cardiovasc Imaging. 2020;21(1):10-21.
56. Nagata Y, Wu VC, Kado Y, Otani K, Lin FC, Otsuji Y, et al. Prognostic Value of Right Ventricular Ejection Fraction Assessed by Transthoracic 3D Echocardiography. Circ Cardiovasc Imaging. 2017;10(2).
57. Li Y, Zhang L, Gao Y, Wan X, Xiao Q, Zhang Y, et al. Comprehensive Assessment of Right Ventricular Function by Three-Dimensional Speckle-Tracking Echocardiography: Comparisons with Cardiac Magnetic Resonance Imaging. J Am Soc Echocardiogr. 2021;34(5):472-82.
58. Laser KT, Karabiyik A, Körperich H, Horst JP, Barth P, Kececioglu D, et al. Validation and Reference Values for Three-Dimensional Echocardiographic Right Ventricular Volumetry in Children: A Multicenter Study. J Am Soc Echocardiogr. 2018;31(9):1050-63.
59. Maffessanti F, Muraru D, Esposito R, Gripari P, Ermacora D, Santoro C, et al. Age-, body size-, and sex-specific reference values for right ventricular volumes and ejection fraction by three-dimensional echocardiography: a multicenter echocardiographic study in 507 healthy volunteers. Circ Cardiovasc Imaging. 2013;6(5):700-10.
60. Muraru D, Spadotto V, Cecchetto A, Romeo G, Aruta P, Ermacora D, et al. New speckle-tracking algorithm for right ventricular volume analysis from three-dimensional echocardiographic data sets: validation with cardiac magnetic resonance and comparison with the previous analysis tool. Eur Heart J Cardiovasc Imaging. 2016;17(11):1279-89.
61. Eroğlu AG, Gökalp S, Atik SU, Önal D, Acar HC, Saltık L. Evaluation of ventricular function and myocardial deformation in children with repaired tetralogy of Fallot by real-time three-dimensional (four-dimensional) echocardiography. Cardiol Young. 2022;32(12):1901-9.
62. Tokodi M, Staub L, Budai Á, Lakatos BK, Csákvári M, Suhai FI, et al. Partitioning the Right Ventricle Into 15 Segments and Decomposing Its Motion Using 3D Echocardiography-Based Models: The Updated ReVISION Method. Front Cardiovasc Med. 2021;8:622118.
63. Song FY, Shi J, Guo Y, Zhang CJ, Xu YC, Zhang QL, et al. Assessment of biventricular systolic strain derived from the two-dimensional and three-dimensional speckle tracking echocardiography in lymphoma patients after anthracycline therapy. Int J Cardiovasc Imaging. 2017;33(6):857-68.

64. Liu BY, Wu WC, Zeng QX, Liu ZH, Niu LL, Tian Y, et al. The value of three-dimensional echocardiography in risk stratification in pulmonary arterial hypertension: a cross-sectional study. Int J Cardiovasc Imaging. 2020;36(4):577-84.
65. Lv Q, Sun W, Wang J, Wu C, Li H, Shen X, et al. Evaluation of Biventricular Functions in Transplanted Hearts Using 3-Dimensional Speckle-Tracking Echocardiography. J Am Heart Assoc. 2020;9(10):e015742.
66. Chen R, Zhu M, Amacher K, Wu X, Sahn DJ, Ashraf M. Non-invasive Evaluation of Right Ventricular Function with Real-Time 3-D Echocardiography. Ultrasound Med Biol. 2017;43(10):2247-55.
67. Bidviene J, Muraru D, Kovacs A, Lakatos B, Ereminiene E, Liptai C, et al. Global and regional right ventricular mechanics in repaired tetralogy of Fallot with chronic severe pulmonary regurgitation: a three-dimensional echocardiography study. Cardiovasc Ultrasound. 2021;19(1):28.
68. Cho EJ, Jiamsripong P, Calleja AM, Alharthi MS, McMahon EM, Khandheria BK, et al. Right ventricular free wall circumferential strain reflects graded elevation in acute right ventricular afterload. Am J Physiol Heart Circ Physiol. 2009;296(2):H413-20.
69. Moceri P, Duchateau N, Gillon S, Jaunay L, Baudouy D, Squara F, et al. Three-dimensional right ventricular shape and strain in congenital heart disease patients with right ventricular chronic volume loading. Eur Heart J Cardiovasc Imaging. 2021;22(10):1174-81.
70. Atsumi A, Seo Y, Ishizu T, Nakamura A, Enomoto Y, Harimura Y, et al. Right Ventricular Deformation Analyses Using a Three-Dimensional Speckle-Tracking Echocardiographic System Specialized for the Right Ventricle. J Am Soc Echocardiogr. 2016;29(5):402-11 e2.
71. Lakatos B, Tősér Z, Tokodi M, Doronina A, Kosztin A, Muraru D, et al. Quantification of the relative contribution of the different right ventricular wall motion components to right ventricular ejection fraction: the ReVISION method. Cardiovasc Ultrasound. 2017;15(1):8.
72. Surkova E, Kovács A, Lakatos BK, Tokodi M, Fábián A, West C, et al. Contraction patterns of the systemic right ventricle: a three-dimensional echocardiography study. Eur Heart J Cardiovasc Imaging. 2022;23(12):1654-62.
73. Lakatos BK, Nabeshima Y, Tokodi M, Nagata Y, Tősér Z, Otani K, et al. Importance of Nonlongitudinal Motion Components in Right Ventricular Function: Three-Dimensional Echocardiographic Study in Healthy Volunteers. Journal of the American Society of Echocardiography. 2020;33(8):995-1005.e1.
74. Sato T, Calderon RJ, Klas B, Pedrizzetti G, Banerjee A. Simultaneous Volumetric and Functional Assessment of the Right Ventricle in Hypoplastic Left Heart Syndrome After Fontan Palliation, Utilizing 3-Dimensional Speckle-Tracking Echocardiography. Circ J. 2020;84(2):235-44.
75. Satriano A, Pournazari P, Hirani N, Helmersen D, Thakrar M, Weatherald J, et al. Characterization of Right Ventricular Deformation in Pulmonary Arterial Hypertension Using Three-Dimensional Principal Strain Analysis. J Am Soc Echocardiogr. 2019;32(3):385-93.
76. Addetia K, Uriel N, Maffessanti F, Sayer G, Adatya S, Kim GH, et al. 3D Morphological Changes in LV and RV During LVAD Ramp Studies. JACC Cardiovasc Imaging. 2018;11(2 Pt 1):159-69.
77. Addetia K, Maffessanti F, Muraru D, Singh A, Surkova E, Mor-Avi V, et al. Morphologic Analysis of the Normal Right Ventricle Using Three-Dimensional Echocardiography-Derived Curvature Indices. J Am Soc Echocardiogr. 2018;31(5):614-23.
78. Bidviene J, Muraru D, Maffessanti F, Ereminiene E, Kovács A, Lakatos B, et al. Regional shape, global function and mechanics in right ventricular volume and pressure

overload conditions: a three-dimensional echocardiography study. Int J Cardiovasc Imaging. 2021;37(4):1289-99.
79. Leary PJ, Kurtz CE, Hough CL, Waiss MP, Ralph DD, Sheehan FH. Three-dimensional analysis of right ventricular shape and function in pulmonary hypertension. Pulm Circ. 2012;2(1):34-40.
80. Gibson DG, Brown DJ. Continuous assessment of left ventricular shape in man. Br Heart J. 1975;37(9):904-10.
81. Sheehan FH, Ge S, Vick GW, 3rd, Urnes K, Kerwin WS, Bolson EL, et al. Three-dimensional shape analysis of right ventricular remodeling in repaired tetralogy of Fallot. Am J Cardiol. 2008;101(1):107-13.
82. Kim HK, Kim YJ, Park JS, Kim KH, Kim KB, Ahn H, et al. Determinants of the severity of functional tricuspid regurgitation. Am J Cardiol. 2006;98(2):236-42.
83. Grapsa J, Gibbs JS, Cabrita IZ, Watson GF, Pavlopoulos H, Dawson D, et al. The association of clinical outcome with right atrial and ventricular remodelling in patients with pulmonary arterial hypertension: study with real-time three-dimensional echocardiography. Eur Heart J Cardiovasc Imaging. 2012;13(8):666-72.
84. Zandstra TE, Jongbloed MRM, Widya RL, Ten Harkel ADJ, Holman ER, Mertens BJA, et al. Validation and Feasibility of Echocardiographic Assessment of Systemic Right Ventricular Function: Serial Correlation With MRI. Front Cardiovasc Med. 2021;8:644193.

Appendix 2: Abstract EuroEcho

Submitted to the EuroEcho-Imaging 2024 congress.

Quantifying Right Ventricular Function in Tetralogy of Fallot: 3D Echo into Longitudinal, Radial, and Anteroposterior Directions

Authors

J.W. Schneijdenberg[a b], R.R. Zwaan[a], Y. Chen[a], D.J. Bowen[a], G. van Burken[a], J.G. Bosch[a] and A.E. van den Bosch[a].

Affiliations

[a] Erasmus MC, Cardiovascular Institute, Thorax Center, Department of Cardiology

[b] Educational program Technical Medicine; Leiden University Medical Center, Delft University of Technology & Erasmus University Medical Center Rotterdam.

Introduction: Tetralogy of Fallot (ToF) is a congenital heart disease requiring surgical correction in early childhood. Despite high surgical success rates, patients cope with severe morbidity during adulthood predominantly originating from the right ventricle (RV). Pathophysiological processes underlying these conditions remain largely unknown, but are mostly attributed to RV remodelling. Improved understanding of remodelling patterns is essential for advancements in clinical decision making and treatment planning.
Purpose: To gain better insight in RV remodelling in patients with ToF, a method for detailed quantification of directional components of RV function was developed using three-dimensional echocardiography (3DE).
Methods: From RV-focused 3DE studies of 50 ToF patients and 50 healthy controls, three-dimensional dynamic RV meshes were obtained using commercially available software (TomTec 4D RV-Function). Within an in-house developed software application (RV-Dynamics), a technique was realized to decompose RV contraction in longitudinal (LT), radial (RD), and anteroposterior (AP) motion directions (Figure 1). Their relative contributions to RV ejection fraction (RVEF) were calculated as measure for RV function, analysed, and statistically compared within and between ToF patients and healthy controls.
Results: Decomposed RVEF in the AP motion direction was identified as the largest relative contributor to RVEF in both ToF patients (38% [31 – 42]) and healthy controls (40% [37 – 44]). Moreover, the AP component was significantly reduced in ToF patients compared to healthy controls (p=0.004). Deterioration in AP direction was complemented by a significant increase of the LT RVEF component (p=0.009), with 28% [26 – 33] in ToF patients compared to 26% [23 – 31] in healthy controls. Relative contribution of RD motion remained the same between both groups (p=0.649) (Figure 2).
Conclusion: RV-Dynamics allowed for effective directional decomposition of RVEF, enabling detailed quantification of RV function in patients with ToF. The AP component proved to be the largest relative contributor to RVEF in both ToF patients and healthy controls, disputing currently applied parameters focussing on LT wall motion for RV function assessment. Deterioration of RV function in ToF patients was mostly assigned to decreased contribution of AP wall motion to RVEF. We hypothesised this relates to the crucial involvement of left ventricular function in RV function, as RV motion in AP direction is largely attributed to left ventricular systolic function. A compensatory increase in LT contraction was observed, suggesting RV remodelling in LT direction in ToF patients.

Keywords: Tetralogy of Fallot; Right Ventricle; Three-Dimensional Echocardiography

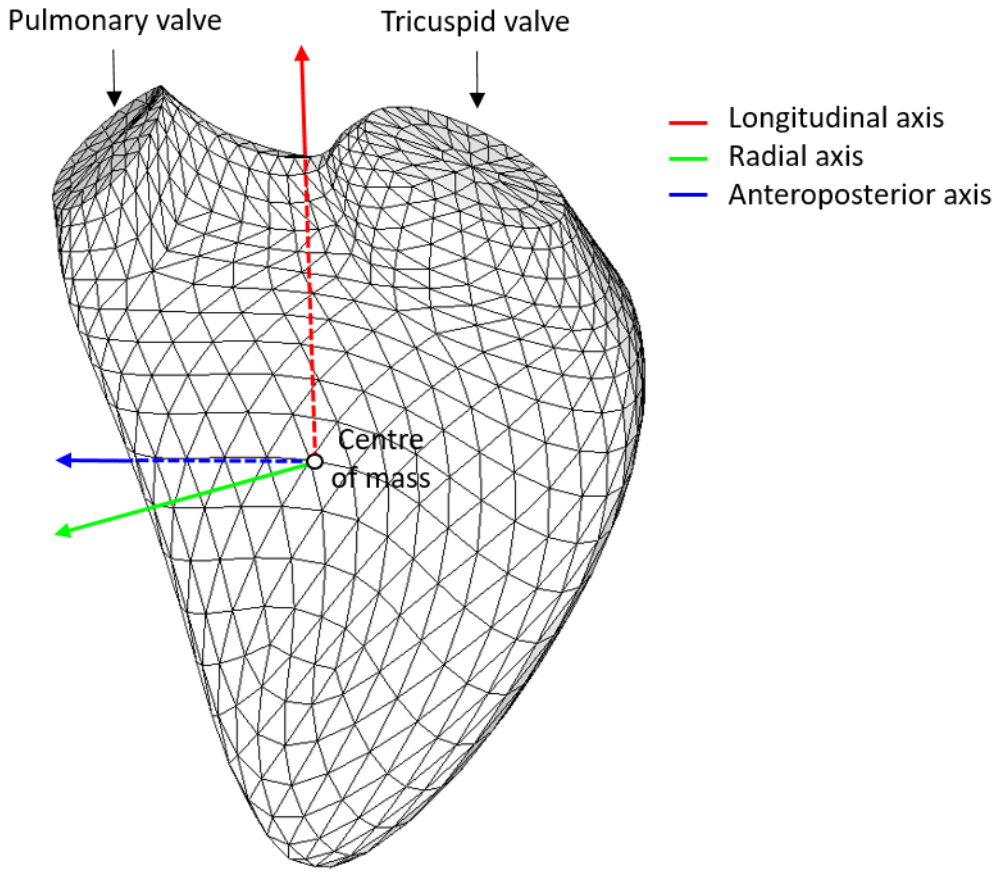

Figure 1: Axis definition and orientation of the three-dimensional dynamic right ventricle mesh. Longitudinal (red), radial (green) and anteroposterior (blue) axes are depicted after translation, locating the origin on the centre of mass of the right ventricle during systole.

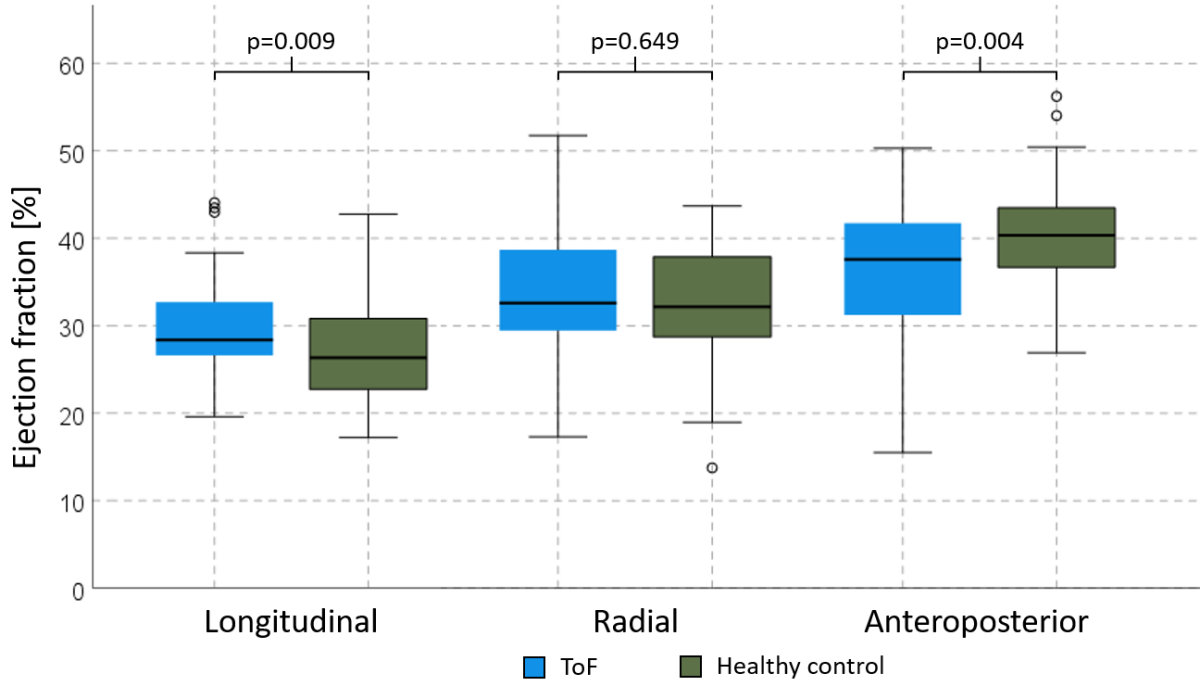

Figure 2: Boxplot comparing relative contributions of decomposed ejection fraction in longitudinal, radial, and anteroposterior directions between Tetralogy of Fallot (ToF) patients and healthy controls.